Constitutive HIF-1α Expression in the Epidermis Fuels Proliferation and Is Essential for Effective Barrier Formation

JID Open

Julia Boix[1,2,12], Jana Knuever[1,3,12], Nadine Niehoff[1], Ayesha Sen[1], David Pla-Martin[1,2,4], Olivier R. Baris[5], Julia Etich[6], Bent Brachvogel[2,6,7], Harshita Kaul[7], Dirk Isbrandt[2,8,9], Ekaterina Soroka[3,7], Hisham Bazzi[2,3,7], Roland H. Wenger[10], Patrick Giavalisco[11] and Rudolf J. Wiesner[1,2,7]

Epidermis is one of the most rapidly proliferating tissues in the body with high demands for adenosine triphosphate and cellular building blocks. In this study, we show that to meet these requirements, keratinocytes constitutively express HIF-1α, even in the presence of oxygen levels sufficient for HIF-1α hydroxylation. We previously reported that mice with severe epidermal mitochondrial dysfunction actually showed a hyperproliferative epidermis but rapidly died of systemic lactic acidosis and hypoglycemia, indicating excessive glycolysis. In this work, we interrogated HIF-1α function in glycolysis by its epidermal ablation combined with mitochondrial dysfunction, which resulted in decreased proliferation but even earlier lethality due to a severe barrier defect. Our data demonstrate that HIF-1α is indispensable for maintaining a high aerobic glycolytic flux necessary for supplying energy but also for synthetizing cellular building blocks such as lipids, which are both essential for proliferation as well as barrier formation. HIF-1α is stabilized in keratinocytes in the presence of oxygen by high levels of HIF-1α transcripts, low levels of prolyl-4-hydroxylases (PHD2 and PHD3), and a low cellular a-ketoglutarate/lactate ratio, likely inhibiting prolyl-4-hydroxylase activity. Our data suggest a key role for constitutive HIF-1α expression allowing a Warburg-like metabolism in healthy, highly proliferative keratinocytes, similar to that in tumor cells.

Keywords: Epidermal barrier function, HIF-1α, Lipid synthesis, Mitochondrial DNA, Skin homeostasis

Journal of Investigative Dermatology (2025) **145,** 1683–1692; doi:10.1016/j.jid.2024.09.022

INTRODUCTION

Oxygen levels vary among tissues and can be very low in wounds and in solid tumors. Most if not all cells in the body react to hypoxia by stabilizing hypoxia-inducible transcription factor HIF-1α and/or HIF-2α to cope with an interruption of oxygen supply and restore tissue homeostasis. HIFα subunits are marked for proteasomal degradation by oxygen and α-ketoglutarate (α-KG)–dependent prolyl-4-hydroxylase domain (PHD) enzymes (Schofield and Ratcliffe, 2004). HIF-1, among many other functions, activates a gene expression program that readjusts cellular metabolism with high rates of anaerobic glycolysis, suppressed oxidative phosphorylation (OXPHOS), and stimulated angiogenesis (Fuhrmann and Brüne, 2017). Thus, HIF-1 ultimately serves as the master regulator of energy homeostasis (Semenza, 2009; Semenza, 2012).

HIF-1α protein is constitutively expressed in the basal layer of normal human (Rezvani et al, 2011b) and mouse (Boutin et al, 2008) epidermis, also reviewed in Rezvani et al (2011a) It was claimed that this is due to physiologic hypoxia in the epidermis (Evans et al, 2006) and that skin thus senses environmental hypoxia and contributes to renal erythropoietin production (Boutin et al, 2008). Low oxygen partial pressure (pO_2) in the environmental air is however a condition rarely encountered by mammals, and therefore, this hypothesis was severely questioned (Paus et al, 2009). Rasmussen et al (2012) later demonstrated that after exposure of human subjects to either systemic or skin hypoxia, the skin does not contribute to erythropoietin expression.

[1]*Center for Physiology and Pathophysiology, Institute of Systems Physiology, University of Köln, Köln, Germany;* [2]*Center for Molecular Medicine Cologne, University of Köln, Köln, Germany;* [3]*Department of Dermatology and Venereology, University Hospital of Köln, Köln, Germany;* [4]*Institute of Biochemistry and Molecular Biology I, University Hospital Düssledorf, Heinrich Heine University Düsseldorf, Düsseldorf, Germany;* [5]*University of Angers, MitoLab, Unité MitoVasc, UMR CNRS 6015, INSERM U1083, SFR ICAT, Angers, France;* [6]*Experimental Neonatology, Department of Pediatrics and Adolescent Medicine, Faculty of Medicine and University Hospital Cologne, University of Cologne, Cologne, Germany;* [7]*Cologne Excellence Cluster on Cellular Stress Responses in Aging-associated Diseases (CECAD), University of Köln, Köln, Germany;* [8]*Institute for Molecular and Behavioral Neuroscience, Faculty of Medicine, University of Köln, Köln, Germany;* [9]*German Center for Neurodegenerative Diseases (DZNE), Bonn, Germany;* [10]*Institute of Physiology, University of Zurich, Zurich, Switzerland; and* [11]*Max Planck Institute for Biology of Aging, Cologne, Germany*

[12]*These authors contributed equally to this work.*

Correspondence: Jana Knuever, Department of Dermatology and Venereology, University Hospital of Köln, Kerpener Street 62, Koln 50937, Germany. E-mail: jana.knuever@uk-koeln.de

Abbreviations: α-KG, α-ketoglutarate; ATP, adenosine triphosphate; OXPHOS, oxidative phosphorylation; PHD, prolyl-4-hydroxylase domain; pO_2, oxygen partial pressure

Received 29 June 2023; revised 15 September 2024; accepted 30 September 2024; accepted manuscript published online 22 November 2024; corrected proof published online 13 December 2024

In addition, pO_2 is not particularly low in the skin (reviewed in Keeley and Mann [2019]), and no hypoxic region was detected in the epidermis using penetrating oxygen electrodes (Baumgärtl et al, 1987), further questioning both the mechanism and the role for constitutive HIF-1α stabilization. Indeed, no obvious skin phenotype was reported in HIF^{eko} mice (Boutin et al, 2008), and only after 6 months were moderate skin atrophy and pruritic inflammation observed with dysregulation of several basal lamina proteins (Rezvani et al, 2011). In addition, it was shown that in the absence of HIF-1α, tissue damage upon UVB irradiation is aggravated (Faßbender et al, 2022). In addition, ablation of HIF-1α in the epidermis prevents tumorigenesis but, at the same time, triggers the formation of hyperkeratotic plaques in later life of mice (Mahfouf et al, 2019). Finally, bacterial infection–induced hypoxia drives increased glutamine metabolism in keratinocytes with attendant enhancement of skin and hair follicle regeneration (Wang et al, 2023).

The epidermis is one of the most rapidly proliferating normal tissues in the body. Dividing and differentiating keratinocytes require a constant supply of energy and building material to produce cellular building blocks. Our previous studies have shown that keratinocytes in the basal epidermal layer are rich in mitochondria (Hornig-Do et al, 2007; Knuever et al, 2012), but others proposed that epidermal energy metabolism is functionally anaerobic, on the basis of high lactate production of epidermal sheets, which is not further increased under hypoxia (Ronquist et al, 2003). Therefore, adenosine triphosphate (ATP) production may not be the only reason for the high mitochondrial content in the basal layer but also the synthesis of pyrimidine nucleotides and membrane lipids for daughter cells, less well-known but essential mitochondrial functions (Wallace, 2012). Consequently, we previously studied mitochondrial function in the epidermis by genetically interfering with mtDNA transcription ($TFAM^{eko}$ mice) (Baris et al, 2011) or mtDNA replication in mice expressing the dominant-negative mutant K320E of the mitochondrial helicase Twinkle (K320E-$Twinkle^{epi}$ mice) (Weiland et al, 2018). We observed no major differentiation defects in the absence of the OXPHOS system but disturbed development of ectodermal appendages, such as hair follicles, sebaceous glands (Kloepper et al, 2015), or teeth pulps (Imhof et al, 2020), which have even higher biomass production rates. Although OXPHOS was absent in K320E-$Twinkle^{epi}$ epidermis, a hyperproliferation of keratinocytes was observed, accompanied by a delay in barrier maturation. Animals died within 1 week after birth, owing to a complex combination of factors, including high lactate levels in the blood, hypoglycemia, and increased expression of proinflammatory cytokines (Weiland et al, 2018). Interestingly, upregulation of *Hif1**a*** gene expression and HIF-1 target genes was observed in the mutant epidermis.

To reveal the role of HIF-1α in epidermal homeostasis, we challenged its function by ablating *Hif1**a*** in K320E-$Twinkle^{epi}$ mice (called $TwinkleHIF^{epi}$ mice). These mice died even earlier owing to severely disturbed lipid deposition with a profound barrier defect followed by an aggravated inflammatory phenotype. Thus, constitutively expressed HIF-1α is not only necessary for the Warburg-like aerobic–glycolytic energy metabolism of the highly proliferative keratinocytes, similar to tumor cells, but also contributes to the formation of a competent epidermal barrier.

We find that HIF-1α is stabilized in the epidermis by high expression levels of the *Hif1**a*** gene, low levels of PHD2/3, and a low intracellular α-KG /lactate ratio, which further inhibits the capacity of PHDs for HIF-1α degradation.

RESULTS

HIF-1α is highly expressed in the well-oxygenated epidermis as well as in cultured keratinocytes

In vivo measurements of local pO_2 in normal mouse skin demonstrated values no lower than 30 Torr in the dermis (40 ± 10 Torr), and most importantly, no hypoxic zone was observed in the epidermis (Figure 1a). *Hif1**a*** mRNA levels were 20-fold higher in mouse epidermis than in the dermis (Figure 1b), and the protein was readily detectable in keratinocytes, even when a high pericellular pO_2 was ensured by cultivation of primary cells on plates with gas-permeable bottoms (Figure 1c) (Wenger et al, 2015). HIF-1α levels further increased under hypoxia and also upon increasing cell density, which decreases oxygen availability (Figure 1c) (Cho et al, 2008)). Therefore, constitutive expression of the generally highly unstable HIF-1α protein in keratinocytes is not due to a hypoxic environment.

$TwinkleHIF^{epi}$ mice die immediately after birth, although low lactate and high glucose levels are restored in the absence of HIF-1α

To understand the role of HIF-1α in epidermal metabolism, we generated *Hif1**a***-knockout mice in a background of mitochondrial dysfunction. Successful knockout was confirmed by RT-qPCR and immunoblotting (Supplementary Figure S1a and b). $TwinkleHIF^{epi}$ mice were born in expected Mendelian ratios but died at postnatal days 0–1, whereas $Twinkle^{epi}$ mice lived until postnatal days 5–8. Mice with an epidermal ablation of *Hif1a* alone (HIF^{eko} mice) survived, similar to controls (Figure 2a). As observed before, expression of K320E-Twinkle in $TwinkleHIF^{epi}$ mice resulted in a 5-fold decrease of mtDNA copy number and 10-fold decrease of a representative mtDNA encoded mRNA (mtCo3), leading to decreased levels of subunits representing the 4 OXPHOS complexes containing mtDNA encoded subunits (complex II containing no such subunits) (Supplementary Figure S1c–e). Complexes I–IV remained normal in HIF^{eko} mice (Supplementary Figure S2b–d), showing that constitutively expressed HIF-1α does not suppress mitochondrial biogenesis in the epidermis, as observed in other cell types (Fuhrmann and Brüne, 2017).

However, the severe hypoglycemia and increased blood lactate levels already present at birth (Figure 2b and c) caused by mitochondrial dysfunction in $Twinkle^{epi}$ mice (for later time points, see Weiland et al [2018]) were normalized in $TwinkleHIF^{epi}$ mice, indicating that factors additional to lactic acidosis contribute to their short life span. Lactate and pyruvate levels in fresh frozen epidermal

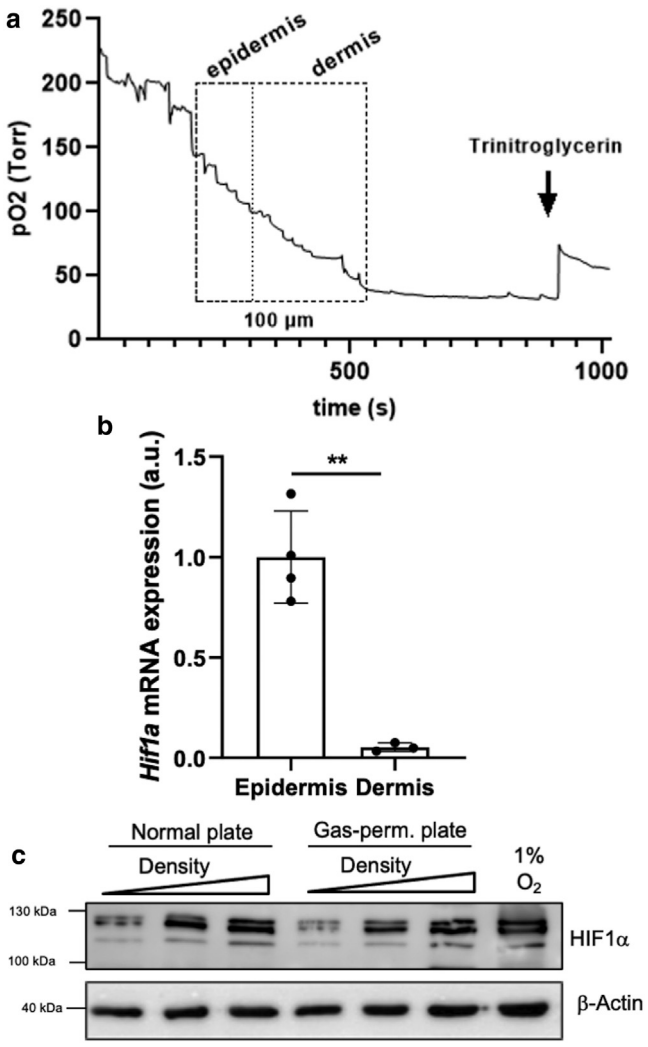

Figure 1. HIF-1α is highly expressed in the well-oxygenated epidermis as well as in cultured keratinocytes. (**a**) Representative graph of local pO_2 measured with a microelectrode inserted in vertical 10-μm steps into mouse scalp skin. Epidermal and dermal layers are indicated, and an increase in pO_2 after NO-mediated vasodilation by glycerol trinitrate application is shown as positive control. (**b**) RT-qPCR showing *Hif1**a*** mRNA levels in epidermis (n = 4) and dermis (n = 3). Data are presented as mean ± SD and analyzed with Student's *t*-test. $^{**}P < .01$. (**c**) Immunoblot showing HIF-1α protein in keratinocytes cultured with increasing density on normal and gas-permeable plates. Keratinocytes cultured under hypoxic conditions (1% O_2, 6 h) served as positive control. β-Actin was used as loading control. a.u., arbitrary unit; h, hour; NO, nitric oxide; O_2, oxygen; pO2, oxygen partial pressure; s, second.

tissue were similar in all genotypes, indicating rapid removal of lactate into the systemic blood stream. Low levels of the glycolytic intermediates glucose-6-phosphate, fructose-6-phosphate, and fructose-1,6-bisphosphate in epidermal tissue of Twinkle^{epi} mice are consistent with and mirror the increased glycolytic flux, whereas rather normal levels in TwinkleHIF^{epi} mice confirm the hampered flux in the absence of HIF-1α. High steady-state levels of phosphoenolpyruvate in both genotypes with defective mitochondria are probably due to low levels of fructose-1,6-bisphosphate, a potent activator of pyruvate kinase (see textbooks of biochemistry). HIF^{eko} mice presented blood lactate levels similar to those of controls. Notably, Twinkle^{epi} mice expressed 3 times more *Hif1**a*** mRNA than the controls, but also mRNA levels of HIF-1 targets crucial for glucose metabolism were increased, including pyruvate dehydrogenase kinase 4 (4.7-fold), hexokinase 2 (2.1-fold), and *Glut1*/*Slc2a1* (1.5-fold) (Figure 2d). These data suggest that epidermis in Twinkle^{epi} mice adapts to the OXPHOS defect by augmentation of *Hif1**a*** gene expression, followed by downstream key glycolysis genes as HIF targets, which however leads to fatal systemic lactic acidosis. In TwinkleHIF^{epi} mice, the expression of all 3 genes was considerably lower than in Twinkle^{epi} newborns (0.8-fold, 0.6-fold, and 0.7-fold, respectively), and hexokinase 2 and *Scl2a1* mRNA was even lower than in controls, showing that constitutively stabilized HIF-1α is essential for maintaining the normal epidermal aerobic–glycolytic program. Significantly low levels of *Scl2a1* mRNA in HIF^{eko} mice support these findings. Twinkle^{epi} mice also showed upregulation of neovascularization genes such as *Adm* (9.9-fold) and *Vegfa* (2.7-fold), but their expression was normalized to control levels in the absence of HIF-1α (Figure 2e), further supporting HIF-1α activation in the absence of functional mitochondria.

The aerobic–glycolytic phenotype of the epidermis was confirmed by measuring the extracellular acidification rate (proportional to lactate production) (Supplementary Figure S3a). Although they proliferate slower in vitro than fibroblasts, wild-type keratinocytes produced 3 times more lactate and consumed 75% more oxygen, consequently showing a 75% higher rate of ATP production by OXPHOS (Supplementary Figure S3b–f). In summary, these data confirm that constitutively stabilized HIF-1α is essential for maintaining an aerobic–glycolytic metabolism of the epidermis. Upon OXPHOS impairment, upregulation of *Hif1**a*** followed by HIF-1 target genes activate compensatory mechanisms to maintain energy homeostasis.

Proliferation and differentiation are impaired in TwinkleHIF^{epi} mice

Histologically, no major skin differentiation defects were observed in all mutant mice at birth (Figure 3). In addition, dermal thickness was similar in all strains (Supplementary Figure S4a). However, the basal proliferative layer showed a significant reduction in the number of Ki-67–positive keratinocytes in the TwinkleHIF^{epi} double-mutant as well as in the HIF^{eko} mice (Figure 3b), leading to a 50% decrease in total epidermal thickness (Figure 3a). Twinkle^{epi} showed no differences to controls in epidermal thickness or keratinocyte proliferation, but HIF^{eko} presented levels similar to those of TwinkleHIF^{epi} mice. Keratin 14 and keratin 10 intensity was reduced in Twinkle^{epi} and TwinkleHIF^{epi} mice (Figure 3c and d). Staining for loricrin (Figure 3e) was reduced in TwinkleHIF^{epi} mice, whereas filaggrin staining intensity was similar in all genotypes (Supplementary Figure S4c). The early proliferation defect in HIF^{eko} mice was compensated later because adult mice had normal epidermal thickness (Supplementary Figure S4b).

In stark contrast, Twinkle^{epi} keratinocytes even proliferate faster, probably fueled by activating aerobic glycolysis upon OXPHOS impairment (Figure 3b) (for later time points, see

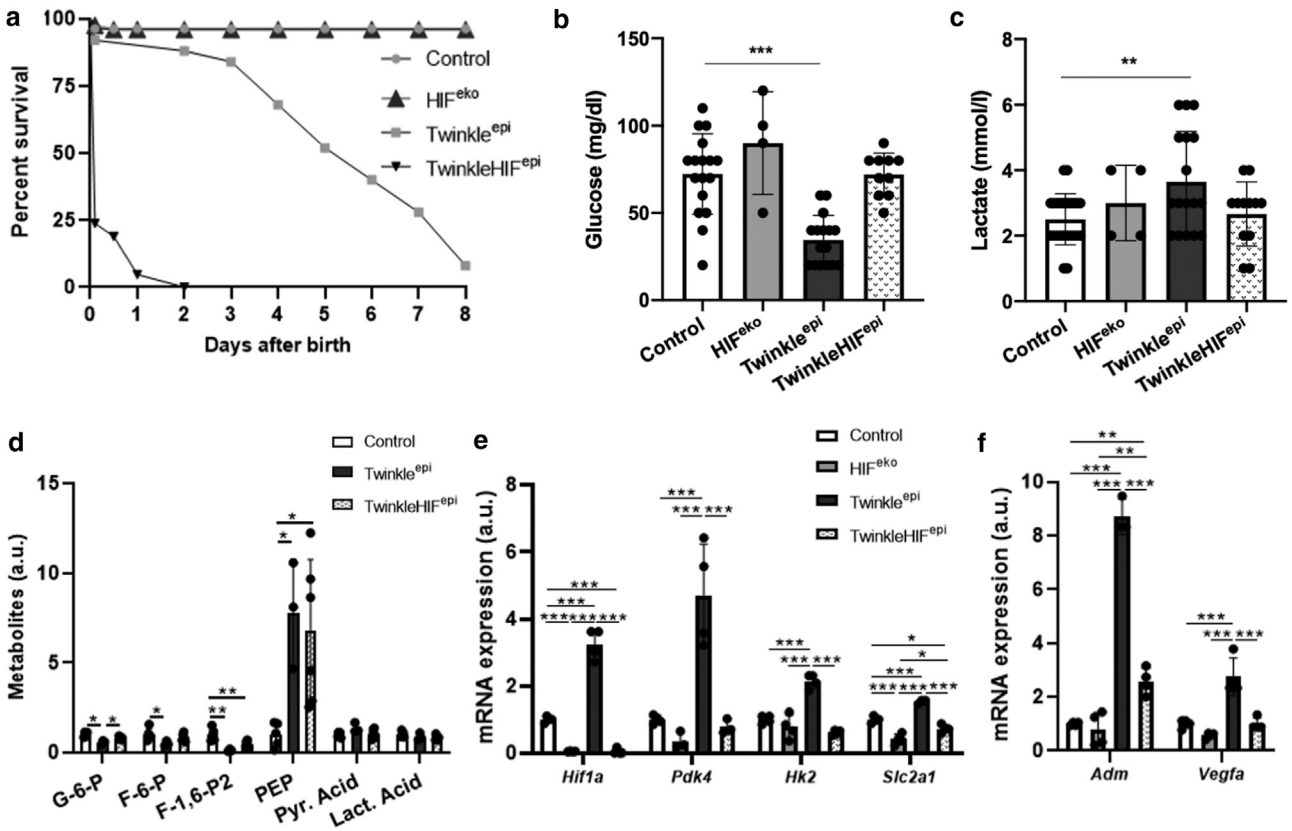

Figure 2. TwinkleHIF^{epi} mice die immediately after birth, although low lactate and high glucose levels are restored in the absence of HIF-1α. (**a**) Graph showing the percentage of surviving control, HIF^{eko}, Twinkle^{epi}, and TwinkleHIF^{epi} mice after birth (n = 20–50 mice per genotype). Blood (**b**) glucose and (**c**) lactate levels in control (n = 24), HIF^{eko} (n = 4), Twinkle^{epi} (n = 17), and TwinkleHIF^{epi} (n = 12) newborn mice. (**d**) Levels of glycolytic intermediates in fresh frozen epidermal tissue from control (n = 4), Twinkle^{epi} (n = 5), and TwinkleHIF^{epi} (n = 6) newborn mice (no tissue was available for HIF^{eko} mice). (**e**) RT-qPCR showing *Hif1a*, *Pdk4*, *Hk2*, *Slc2a1*, and (**f**) *Adm* and *Vegfa* mRNA levels in control, HIF^{eko}, Twinkle^{epi}, and TwinkleHIF^{epi} newborn epidermis at birth (n = 3–8 mice per genotype). Data are presented as mean ± SD, analyzed with 1-way ANOVA, Tukey's posthoc test. *$P < .05$, **$P < .01$, and ***$P < .001$. a.u., arbitrary unit; Hk2, hexokinase 2; Pdk4, pyruvate dehydrogenase kinase 4.

Weiland et al [2018]), leading to enhanced epidermal thickness (Figure 3a). Caspase-3–positive cells were observed only in HIF^{eko} mice (Supplementary Figure S5c and e).

These data suggest that constitutive HIF-1α expression is mandatory to maintain a sufficiently high production rate of ATP and of cellular building blocks for epidermal proliferation and survival, whereas a mitochondrial defect in the presence of HIF-1α can be compensated.

TwinkleHIF^{epi} mice show an epidermal maturation delay and a severe barrier defect

TwinkleHIF^{epi} mice exhibited small lesions or even wounds in the ventral skin at birth (Figure 4a), suggesting skin fragility, probably induced by mechanical stress upon birth, because such lesions were absent in late embryos. Using toluidine blue, we investigated whether barrier integrity was generally impaired. At postnatal day 0, no general penetration of the dye was observed in skin of controls, whereas lesions were stained in TwinkleHIF^{epi} mice (Figure 4b), needless to say. At embryonic day 17.5, toluidine blue penetration was noted in the entire TwinkleHIF^{epi} ventral skin but not in the controls, indicating a delay in epidermal maturation. The same assay revealed only a mild maturation delay in Twinkle^{epi} mice, which was completely resolved at birth (Weiland et al, 2018).

TwinkleHIF^{epi} mice showed a 2.2-fold increase in transepidermal water loss (Figure 4c) and a significant reduction in body weight compared with that in all other strains (Figure 4d), indicating a severe disruption of the inside-out barrier function as well. A proper epidermal barrier is mainly supported by a network of keratins and cornified envelope proteins such as filaggrin, loricrin or small proline rich proteins, tight junctions (containing claudins) as well as lipids (ceramides, free fatty acids, and cholesterol), which together build the stratum corneum (Segre, 2006; van Smeden and Bouwstra, 2016). Probably as a compensatory response, *Sprr2d*, *Sprr2h*, and *Cldn4* mRNAs were highly increased in TwinkleHIF^{epi} epidermis (13.6-, 5.9-, and 4.0-fold, respectively) but less in Twinkle^{epi} than in the controls or HIF^{eko} mice (Figure 4e). Nonetheless, upregulation of these epidermal differentiation cluster genes failed to compensate the severe barrier defect when HIF-1α and functional mitochondria were absent.

Both functional mitochondria and HIF-1α are required for proper lipid deposition

Nilered staining of polar (red) and nonpolar (green) lipids showed that whereas all stratum corneum layers mainly contain polar lipids in control and Twinkle^{epi} mice, their

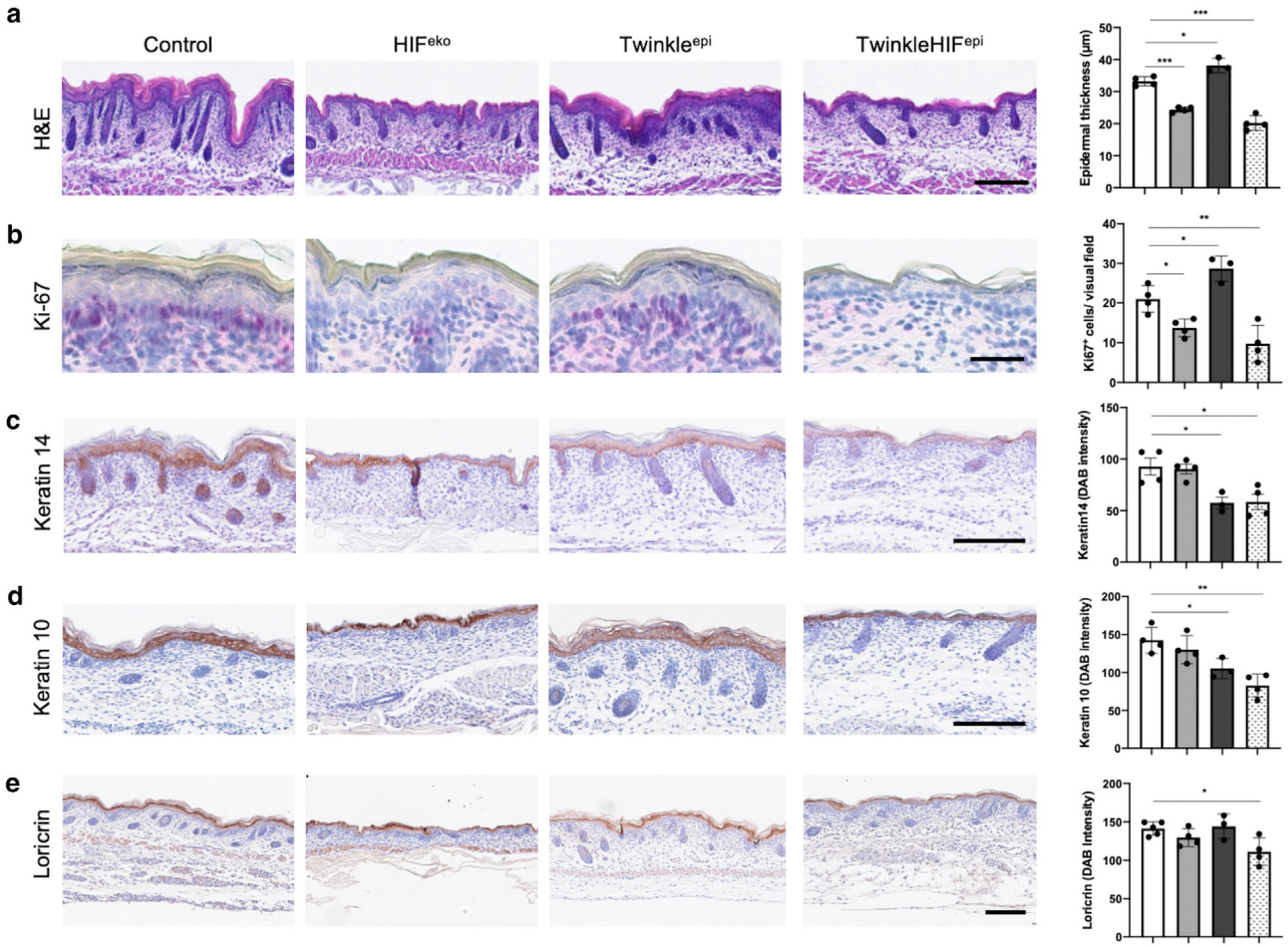

Figure 3. Proliferation and differentiation are impaired in TwinkleHIF^{epi} mice. (**a**) H&E staining and quantification of epidermal thickness. (**b**) Immunostaining and quantification of Ki-67–positive keratinocytes. Bar = 50 μm. Immunostaining and quantification of (**c**) keratin 14, (**d**) keratin 10, and (**e**) loricrin of control, HIF^{eko}, Twinkle^{epi} (n = 3), and TwinkleHIF^{epi} newborn back skin at birth (n = 4 mice per other 3 genotypes). Bar = 200 μm (**a** and **c**–**e**). Data are presented as mean ± SD (for **a**–**e**), analyzed with 1-way ANOVA, Tukey's posthoc test. *$P < .05$, **$P < .01$, and ***$P < .001$.

content was significantly reduced in HIF^{eko} and TwinkleHIF^{epi} mice (Figure 5a and b). This demonstrates a severe defect in the synthesis and/or deposition of polar lipids in the absence of HIF-1α and/or dysfunctional mitochondria. Hence, we analyzed the expression of the key enzymes in the synthesis pathways of the 3 main polar lipid classes of the stratum corneum (Figure 5c): elongation of very-long-chain fatty acids protein 3 (*Elovl3*), *Pla2g5*, and cathepsin E (*Ctse*) (Pappas, 2009; Segre, 2006). In agreement with our staining results, *Elovl3* mRNA was decreased in the epidermis of Twinkle^{epi} and TwinkleHIF^{epi} mice by approximately 75%, *Pla2g5* was downregulated by 40 and 75%, respectively, whereas the decrease in *Ctse* expression was not significant. Expression of *Flg* mRNA, a key protein for proper stratum corneum function, was reduced in TwinkleHIF^{epi} mice only. This result was not corroborated by FLG protein staining (Supplementary Figure S4c). HIF^{eko} mice did not show differences related to controls (Figure 5c and Supplementary Figure S4c).

Because mTORC2 was shown to control lipid synthesis as well as FLG processing during epidermal barrier formation (Ding et al, 2020), we analyzed expression of rictor, an adaptor protein in the mTORC2 complex, which was downregulated in TwinkleHIF^{epi} mice compared with that in the controls (Figure 5c). Moreover, mTORC2 complex activity, analyzed by the phosphorylated protein kinase B/protein kinase B ratio, was clearly lower in TwinkleHIF^{epi} mice at birth than in the controls (Figure 5d and e), possibly contributing to the metabolic disability of the epidermis to form a functioning barrier and lipophilic stratum corneum.

In summary, our data indicate that both proper mitochondrial function and HIF-1α activity are important for adequate expression of enzymes involved in cornified envelope formation, especially in lipid synthesis.

The inflammatory response induced by mitochondrial dysfunction is exaggerated in the absence of HIF-1α

The inflammatory skin phenotype of Twinkle^{epi} mice was due to an increased expression of proinflammatory genes, possibly explained by a release of mitochondrial damage-associated molecular patterns a few days after birth (Weiland et al, 2018). In TwinkleHIF^{epi} mice, the expression of proinflammatory genes was further exacerbated shortly after birth (Supplementary Figure S5a, note the log scale). Whereas the expression of *Il1b* and nitric oxide synthase 2 were comparable

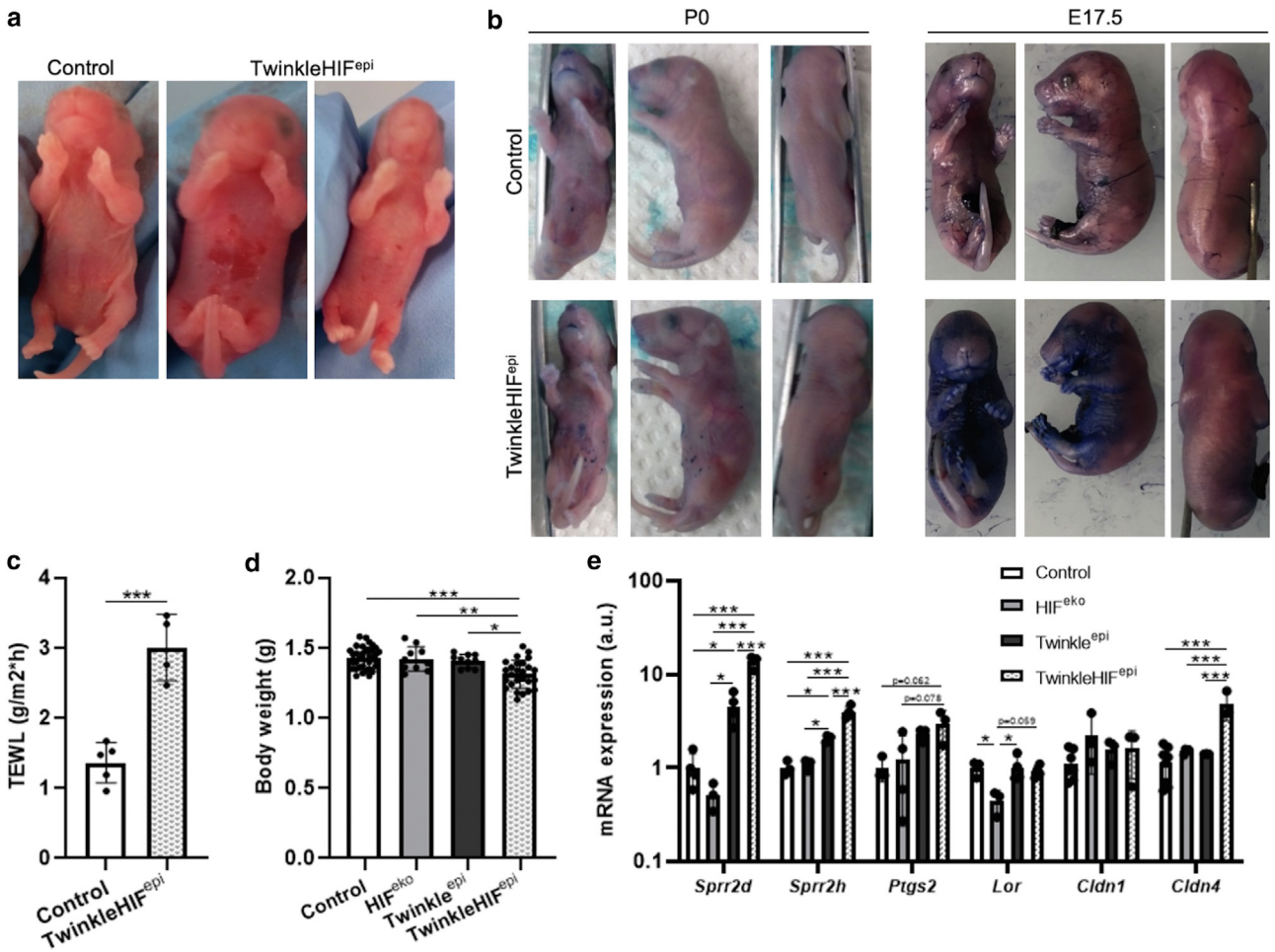

Figure 4. TwinkleHIF^{epi} mice show an epidermal maturation delay and a severe barrier defect. (**a**) Macroscopic ventral view of newborn control and TwinkleHIF^{epi} mice. (**b**) Toluidine blue staining (outside-in epidermal barrier function) at birth (P0) and E17.5 in control and TwinkleHIF^{epi} mice. (**c**) TEWL assessment (inside-out epidermal barrier function) in control and TwinkleHIF^{epi} newborn mice (n = 4–5 mice per genotype). (**d**) Control (n = 36), HIF^{eko} (n = 10), Twinkle^{epi} (n = 10), and TwinkleHIF^{epi} (n = 26) body weight at birth. (**e**) RT-qPCR showing *Sprr2d, Sprr2h, Ptgs2, Lor, Cldn1,* and *Cldn4* mRNA levels in control; HIF^{eko}; Twinkle^{epi}; and TwinkleHIF^{epi} newborn epidermis (n = 3–4 mice per genotype). Data are shown as mean ± SD (for **c**–**e**) analyzed with Student's *t*-test (for **c**) and 1-way ANOVA, Tukey's posthoc test (for **d** and **e**). *$P < .05$, **$P < .01$, and ***$P < .001$. E17.5, embryonic day 17.5; Lor, loricrin; P0, postnatal day 0; TEWL, transepidermal water loss.

with the controls in Twinkle^{epi} mice, TwinkleHIF^{epi} mice showed a 9.9- and 7.8-fold increase, respectively. The expression of *S100a8* and *S100a9* and *Slpi* dramatically increased up to 45, 34, and 28 times in TwinkleHIF^{epi} mice, respectively. Expression of wounding-associated keratin 6b and *Tnfa* was also augmented in TwinkleHIF^{epi} mice (Supplementary Figure S5a), whereas the absence of HIF-1α alone in HIF^{eko} mice had no effect on the expression of all these genes. *Il6* mRNA was undetectable in the epidermis of all 4 genotypes (data not shown), but the IL-6 cytokine was found at high levels in the serum of TwinkleHIF^{epi} mice (Supplementary Figure S5b), showing that the severe barrier defect has caused a systemic response. However, numbers of macrophages (F4/80) and mast cells (Giemsa) were comparable in all 4 genotypes (Supplementary Figure S5c and d), indicating that, at birth, an immune cell infiltrate had not yet been recruited. These data indicate that epidermal and systemic inflammation may contribute to the very early death of TwinkleHIF^{epi} mice and is caused by the severe barrier defect.

How is HIF-1α constitutively stabilized under normoxic conditions?

Under normoxia, HIF-1α is hydroxylated by PHDs and degraded by the proteasome (Schofield and Ratcliffe, 2004), whereas at low oxygen availability, PHD activity is inhibited, and consequently, HIF-1α is stabilized. However, other factors and metabolites additionally modulate PHD function, allowing for HIF-1α stabilization independent of oxygen (Fuhrmann and Brüne, 2017; Semenza, 2012).

We thus first hypothesized that HIF-1α stabilization was related to high ROS levels present in human keratinocytes (Hornig-Do et al, 2007) because ROS have recently been shown to oxidatively inactivate PHDs (Lee et al, 2020). Hence, we incubated keratinocytes with trolox and N-acetylcystein, 2 powerful ROS scavengers (Aldini et al, 2018; Cordes et al, 2009; Deneke, 2000; Kitasaka et al, 2020), but observed no relevant effect, neither on HIF-1α protein or mRNA levels nor on expression of HIF-1 target genes (Supplementary Figure S6a and b).

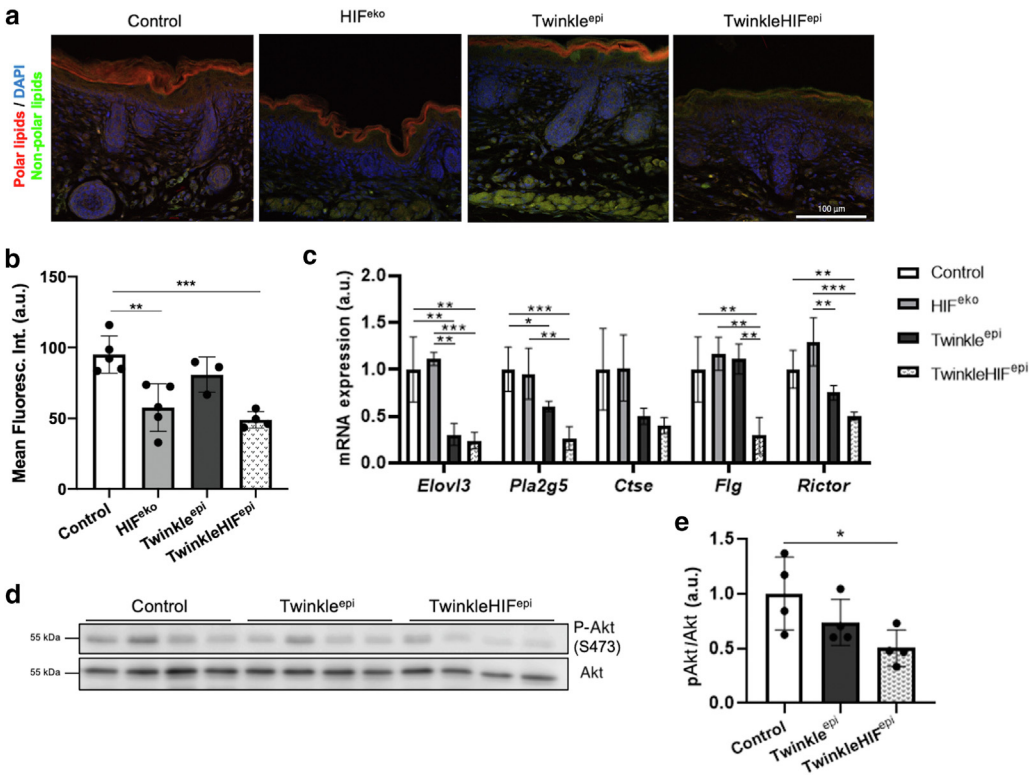

Figure 5. Both functional mitochondria and HIF-1α are required for proper lipid deposition. (**a**) Nilered staining and (**b**) quantification of polar lipids in newborn control (n = 5), HIF^{eko} (n = 5), Twinkle^{epi} (n = 3), and TwinkleHIF^{epi} (n = 4) skin. polar lipids, red; nonpolar lipids, green; and DAPI, blue. Bar = 100 μm. (**c**) RT-qPCR showing *Elovl3*, *Pla2g5*, *Ctse*, *Flg*, and *Rictor* mRNA levels in control; HIF^{eko}; Twinkle^{epi}; and TwinkleHIF^{epi} newborn epidermis (n = 3–4 mice per genotype). (**d**) Immunoblot of pAKT and Akt and (**e**) quantification in control, Twinkle^{epi}, and TwinkleHIF^{epi} epidermal sheets (n = 4 mice per genotype). Data are presented as mean ± SD (for **b, c,** and **e**) and analyzed with 1-way ANOVA, Tukey's posthoc test. *$P < .05$, **$P < .01$, and ***$P < .001$. Akt, protein kinase B; a.u., arbitrary unit; pAkt, phosphorylated protein kinase B.

On the other hand, levels of the HIF-1α–degrading enzymes PHD2 and PHD3 were lower in wild-type keratinocytes than in fibroblasts (Figure 6a and b). In addition, HIF-1α stabilization independent of oxygen availability was also demonstrated in cells with high intracellular levels of the tricarboxylic acid cycle metabolites fumarate and succinate and its by-product 2-OH-glutarate. Because α-KG is necessary for PHDs, whereas the other metabolites are inhibiting, we calculated the ratios of α-KG/inhibiting metabolites, assuming that ratios below 1 will inhibit PHDs and stabilize HIF-1α, as shown before (Ryan et al, 2019; Williams et al, 2022; Yogev et al, 2010). The ratios were as follows: a-KG/succinate = 1.82, a-KG/fumarate = 1.17, and a-KG/2-OH-glutarate = 5.04 (Figure 6c, left panel). However, the ratio of a-KG/lactate was 0.14, making the extremely high intracellular lactate concentration a possible candidate. Together with low a-KG/fumarate (0.73) and low a-KG/lactate (0.30) ratios in fresh frozen epidermis (Figure 6c, right panel), we propose that high intracellular lactate and possibly fumarate, together with low levels of PHDs and in combination with high *Hif1a* mRNA (Figure 1b), are responsible for the constitutive epidermal expression of HIF-1α in the presence of oxygen.

DISCUSSION

We found that the highly unstable transcription factor HIF-1α is constitutively expressed in keratinocytes even in the presence of oxygen. In fact, a high steady-state oxygen level in the epidermis in vivo is maintained by oxygen flux from dermal blood vessels, located close to the basement membrane, as well as by oxygen supply from the surrounding air (Stücker et al, 2002, 2000).

Using 3 mouse models, we demonstrate that HIF-1α expression in the epidermis is required for maintaining a constitutively high aerobic–glycolytic flux. When absent in TwinkleHIF^{epi} and HIF^{eko} epidermis, low expression of the glucose transpoter Slc2a1 and of important glycolysis-related target genes, respectively, indicates that the hypoxia-inducible transcription factor is crucial for basal glycolysis gene expression. A high glycolytic flux in the presence of oxygen may be necessary for the high proliferation rate of the basal layer providing ATP but also cellular building blocks, comparable with the Warburg effect observed in many tumor cells with a similar expression profile of metabolic genes (Kierans and Taylor, 2021).

In addition, we show that HIF-1α establishes a potentially compensatory mechanism in the epidermis upon OXPHOS impairment, which occurs in sun-exposed skin areas especially vulnerable to extrinsic aging (Birket and Birch-Machin, 2007; Hudson et al, 2016) and which are due to the accumulation of mtDNA deletions and point mutations.

Twinkle^{epi} mice even showed increased keratinocyte proliferation leading to increased epidermal thickness. In stark

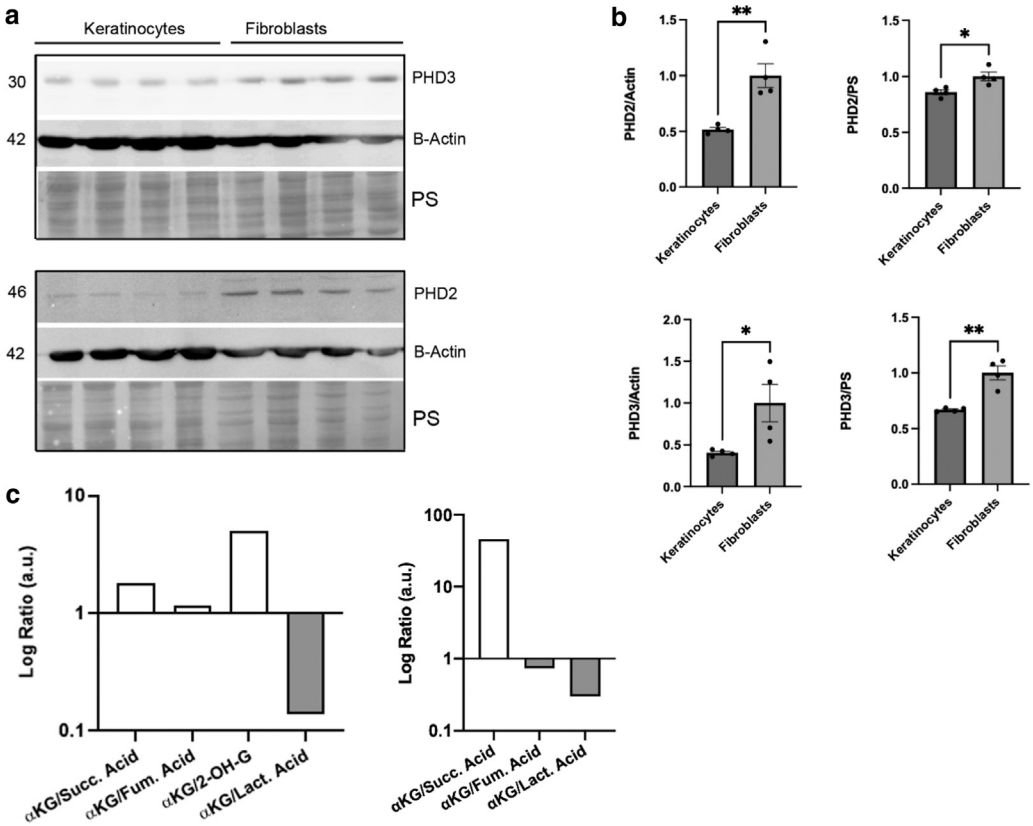

Figure 6. How is HIF-1α constitutively stabilized under normoxic conditions? (**a**) Representative immunoblot of PHD2 and PHD3 and quantification (**b**) in wild-type keratinocytes and fibroblasts. β-Actin and PS were used as loading controls. (**c**) Ratios of metabolites relevant for PHD activity in wild-type keratinocytes (left, n = 4 biological replicates) and wild-type epidermal tissue (right, n = 4 biological replicates). Data are presented as mean ± SD and analyzed with Student's *t*-test. $*P < .05$ and $**P < .01$. PHD, prolyl-4-hydroxylase domain; PS, Ponceau S.

contrast, in TwinkleHIF^{epi} mice, with the same severe mitochondrial defect, the absence of HIF-1α prevented the increase in glycolytic flux necessary to compensate for the OXPHOS defect. This results in diminished keratinocyte proliferation and, consequently, reduction in epidermal thickness. In agreement, hyperproliferative keratinocytes from psoriatic lesions express high levels of hypoxia-inducible factor (Rosenberger, 2007), and human *HIF1a*-knockdown keratinocytes were not able to form a stratified epidermis in vitro and showed reduced proliferation (Rezvani H. R. et al, 2011).

The metabolic defect in TwinkleHIF^{epi} mice causes a delay in epidermal outside-in barrier maturation at embryonic day 17.5. The induced expression of *Sprr2d* and *Sprr2h* at birth in both Twinkle^{epi} and TwinkleHIF^{epi} mouse models is similar to the compensatory mechanism promoting a functional barrier described in loricrin epidermal knockout mice (Huebner et al, 2012). In both genotypes, the outside-in barrier was fully functional at birth except for small ventral lesions found in TwinkleHIF^{epi} mice due to skin fragility. However, the inside-out barrier was severely disturbed in TwinkleHIF^{epi} mice as shown by an impressive water loss resulting in weight loss, likely one cause of early death. Our findings are similar to those of other reported mouse models of disrupted epidermal barrier, for example, HIF-1β epidermal knockout mice showing an impaired barrier and postnatal death due to severe dehydration (Takagi et al, 2003).

Decreased deposition of polar lipids may significantly contribute to the inside-out barrier defect in TwinkleHIF^{epi} mice, similar to that in mice that are deficient in epidermal lipid synthesis enzymes (Pappas, 2009; Segre, 2006). Surprisingly, mitochondrial dysfunction not only causes defective lipid synthesis, as expected, but also reduced expression of enzymes important for the de novo synthesis of barrier lipids (*Elovl3* and *Pla2g5*). In Twinkle^{epi} mice, lipid deposition was not impaired despite downregulation of *Elovl3* and *Pla2g5* mRNAs. HIF^{eko} newborns showed decreased polar lipid deposition but no differences in the expression of lipid synthesis–related genes. We propose that the impairment of both OXPHOS and aerobic glycolysis in TwinkleHIF^{epi} mice leads to compensatory downregulation of these essential genes to reduce the metabolic load of synthetizing extracellular lipids.

As expected, impairment of ATP production in TwinkleHIF^{epi} mice led to mTORC2 inhibition with downregulation of *Rictor* expression and a lower activation state of protein kinase B by phosphorylation (Ser473). Accordingly, the skin phenotype of epidermal *Rictor*-knockout mice (Ding et al, 2020) shares many similarities with that of TwinkleHIF^{epi} mice at birth, including reduced keratinocyte proliferation, epidermal thinning, diminished lipid synthesis and deposition, increased transepidermal water loss, delayed epidermal barrier maturation, and increased proinflammatory cytokine expression. In Twinkle^{epi} mice with augmented glycolytic

flux, neither downregulation of *Rictor* nor diminished protein kinase B activation was observed, also explaining the absence of a barrier defect.

Cytokine induction and inflammation are intrinsic responses to epidermal barrier disruption (Segre, 2006). Skin has been shown to be an important source of systemic cytokines during aging (Hu et al, 2017), when a functional epidermal barrier is compromised owing to defective repair mechanisms (Velarde, 2017). Local and systemic cytokine induction but not epidermal hyperplasia was detected in TwinkleHIF^{epi} mice at birth, most likely due to the loss of HIF-1α and its effect on keratinocyte proliferation, as described in vitro (Rezvani et al, 2011). In conclusion, both the severe epidermal barrier dysfunction and the induction of proinflammatory cytokines probably lead to the premature death of TwinkleHIF^{epi} mice.

Finally, factors other than hypoxia are obviously responsible for epidermal HIF-1α stabilization, and even in hypoxia, HIF-1α stabilization is mostly not oxidant initiated, as recent findings have shown (Kumar et al, 2021). We find that ROS, altered by ROS scavenger treatment in vitro, neither impact *Hif1**a*** mRNA nor HIF-1α protein levels in keratinocytes. Succinate, fumarate, and 2-OH-glutarate do not reach levels high enough to inhibit PHDs, when related to their substrate a-KG. However, low levels of PHD2 and PHD3 as well as high intracellular lactate may importantly contribute to normoxic HIF-1α stabilization, as previously described (De Saedeleer et al, 2012).

In summary, the metabolic defects seen upon OXPHOS dysfunction in the epidermis are more severe in the absence of HIF-1α, indicating that HIF-1α is necessary for maintaining its basal metabolic phenotype. Our data suggest, to our knowledge, a previously unreported role for HIF-1α as a guardian of epidermal homeostasis through the regulation of keratinocyte aerobic–glycolytic energy metabolism, but equally important also are anabolic reactions necessary for cell division and synthesis of barrier lipids.

MATERIALS AND METHODS

pO_2 in skin in vivo

The local pO_2 in mouse skin was determined using a Clark-type oxygen microelectrode with a tip diameter of 10 μm (Unisense, Copenhagen, Denmark) on 3 consecutive locations on the shaved scalp of 3 anesthetized mice (1–1.5% isoflurane in 100% oxygen). Mice were kept at 37 °C on a homeothermic heating pad with intraauricular fixation in a stereotaxic apparatus (Stoelting, Dublin, Ireland). To avoid oxygen convection into an air-filled channel after skin penetration, the location was sealed with a drop of 0.9% sodium chloride solution. After calibration, the electrode was vertically moved forward into the skin in 10-μm steps using a motorized, computer-controlled stereotaxic instrument (Neurostar, Tübingen, Germany), and pO_2 values were recorded each second. To demonstrate proper responsiveness of the electrode toward oxygen, the blood flow was increased with topically applied glycerol trinitrate (G. Pohl-Boskamp, Hohenlockstedt, Germany).

All animal experiments were approved by the animal care committee of the University of Cologne and local government authorities (Bezirksregierung Köln; Landesamt für Natur, Umwelt und Verbraucherschutz, Recklinghausen; Az.81-02.04.2019.A101; 84-02.04.2015.A405).

All standard Materials and Methods are described in Supplementary Materials and Methods.

DATA AVAILABILITY STATEMENT

All data supporting the conclusions of the manuscript are shown in the corresponding figures and supplements. No large datasets were generated or analyzed.

ORCIDs

Jana Knuever: https://orcid.org/0000-0003-1066-6431
Ayesha Sen: https://orcid.org/0000-0002-8744-4995
Olivier R. Baris: https://orcid.org/0000-0003-0974-6856
Ekaterina Soroka: https://orcid.org/0009-0008-7783-1757
Hisham Bazzi: https://orcid.org/0000-0001-8388-4005
Roland H. Wenger: https://orcid.org/0000-0001-7592-4839
Rudolf J. Wiesner: https://orcid.org/0000-0003-1677-4476

CONFLICT OF INTEREST

The authors state no conflict of interest.

ACKNOWLEDGMENTS

JB, JK, AS, HB, and RJW were supported by the Deutsche Forschungsgemeinschaft (German Research Foundation, project identification 73111208 - SFB 829/A14/A12/Z03 projects). JE and BB were supported by Deutsche Forschungsgemeinschaft to the Research Unit FOR2722 - BR2304/12-1 - 407146744, ET144/3-2384170921, and BR2304/7-1 – 207342459. HB and RJW were also funded by the Cologne Excellence Cluster on Cellular Stress Responses in Aging-associated Diseases. JK was supported by the Koeln Fortune Program, Faculty of Medicine, University of Cologne (465/2019 and 254/2022). ORB was supported by Agence Nationale de la Recherche (ANR-20-CE92-0020-01). The authors thank the Cologne Excellence Cluster on Cellular Stress Responses in Aging-associated Diseases Central Imaging Facility for support. We also acknowledge Bernhard Brüne and Nathalie Dehne, Institute of Biochemistry I, Frankfurt, for the gift of Hif1**a**$^{loxP/loxP}$ mice. We are very grateful to Thomas Streichert, Sven Schmidt, and Elke Dietzel, Institute for Clinical Chemistry, Cologne, for measuring glucose and lactate in our samples. We thank Max Schütter for his work in performing and analyzing metabolomics data and the Frezza lab (Cologne Excellence Cluster on Cellular Stress Responses in Aging-associated Diseases) for continuous discussion of our data and gift of reagents.

AUTHOR CONTRIBUTIONS

Conceptualization: RJW; Formal Analysis: JB, JK, DP-M, PG; Investigation: JB, JK, DP-M, NS, NN, PG; Project Administration: DI, ES, HB, JE, BB, ORB, RHW; Supervision: RJW; Writing – Original Draft Preparation: JB, JK, RJW; Writing – Review and Editing: JB, JK, NN, NS, DP-M, ORB, JE, BB, HK, DI, ES, HB, RHW, PG, RJW

SUPPLEMENTARY MATERIAL

Supplementary material is linked to the online version of the paper at www.jidonline.org, and at https://doi.org/10.1016/j.jid.2024.09.022.

REFERENCES

Aldini G, Altomare A, Baron G, Vistoli G, Carini M, Borsani L, et al. N-acetylcysteine as an antioxidant and disulphide breaking agent: the reasons why. Free Radic Res 2018;52:751–62.

Baris OR, Klose A, Kloepper JE, Weiland D, Neuhaus JF, Schauen M, et al. The mitochondrial electron transport chain is dispensable for proliferation and differentiation of epidermal progenitor cells. Stem Cells 2011;29:1459–68.

Baumgärtl H, Ehrly A, Saeger-Lorenz K, Lübbers D. Initial results of intracutaneous measurements of PO_2 profiles. In: Ehrly AM, Hauss J, Huch R, editors. Clinical oxygen pressure measurement. Berlin, Heidelberg: Springer; 1987. p. 121–8.

Birket MJ, Birch-Machin MA. Ultraviolet radiation exposure accelerates the accumulation of the aging-dependent T414G mitochondrial DNA mutation in human skin. Aging Cell 2007;6:557–64.

Boutin AT, Weidemann A, Fu Z, Mesropian L, Gradin K, Jamora C, et al. Epidermal sensing of oxygen is essential for systemic hypoxic response. Cell 2008;133:223–34.

Cho YS, Bae JM, Chun YS, Chung JH, Jeon YK, Kim IS, et al. HIF-1alpha controls keratinocyte proliferation by up-regulating p21(WAF1/Cip1). Biochim Biophys Acta 2008;1783:323–33.

Cordes T, Vogelsang J, Tinnefeld P. On the mechanism of trolox as antiblinking and antibleaching reagent. J Am Chem Soc 2009;131:5018–9.

De Saedeleer CJ, Copetti T, Porporato PE, Verrax J, Feron O, Sonveaux P. Lactate activates HIF-1 in oxidative but not in Warburg-phenotype human tumor cells. PLoS One 2012;7:e46571.

Deneke SM. Thiol-based antioxidants. Curr Top Cell Regul 2000;36:151–80.

Ding X, Willenborg S, Bloch W, Wickström SA, Wagle P, Brodesser S, et al. Epidermal mammalian target of rapamycin complex 2 controls lipid synthesis and filaggrin processing in epidermal barrier formation. J Allergy Clin Immunol 2020;145:283–300.e8.

Evans SM, Schrlau AE, Chalian AA, Zhang P, Koch CJ. Oxygen levels in normal and previously irradiated human skin as assessed by EF5 binding. J Invest Dermatol 2006;126:2596–606.

Faßbender S, Sondenheimer K, Majora M, Schindler J, Opitz FV, Pollet M, et al. Keratinocytes counteract UVB-induced immunosuppression in mice through HIF-1a signaling. J Invest Dermatol 2022;142:1183–93.

Fuhrmann DC, Brüne B. Mitochondrial composition and function under the control of hypoxia. Redox Biol 2017;12:208–15.

Hornig-Do HT, von Kleist-Retzow JC, Lanz K, Wickenhauser C, Kudin AP, Kunz WS, et al. Human epidermal keratinocytes accumulate superoxide due to low activity of Mn-SOD, leading to mitochondrial functional impairment. J Invest Dermatol 2007;127:1084–93.

Hu L, Mauro TM, Dang E, Man G, Zhang J, Lee D, et al. Epidermal dysfunction leads to an age-associated increase in levels of serum inflammatory cytokines. J Invest Dermatol 2017;137:1277–85.

Hudson L, Bowman A, Rashdan E, Birch-Machin MA. Mitochondrial damage and ageing using skin as a model organ. Maturitas 2016;93:34–40.

Huebner AJ, Dai D, Morasso M, Schmidt EE, Schäfer M, Werner S, et al. Amniotic fluid activates the nrf2/keap1 pathway to repair an epidermal barrier defect in utero. Dev Cell 2012;23:1238–46.

Imhof T, Rosenblatt K, Pryymachuk G, Weiland D, Noetzel N, Deschner J, et al. Epithelial loss of mitochondrial oxidative phosphorylation leads to disturbed enamel and impaired dentin matrix formation in postnatal developed mouse incisor. Sci Rep 2020;10:22037.

Keeley TP, Mann GE. Defining physiological normoxia for improved translation of cell physiology to animal models and humans. Physiol Rev 2019;99:161–234.

Kierans SJ, Taylor CT. Regulation of glycolysis by the hypoxia-inducible factor (HIF): implications for cellular physiology. J Physiol 2021;599:23–37.

Kitasaka S, Yagi M, Kikuchi A. Suppression of Menthyl Anthranilate (UV-A sunscreen)-sensitized singlet oxygen generation by trolox and α-tocopherol. Photochem Photobiol Sci 2020;19:913–9.

Kloepper JE, Baris OR, Reuter K, Kobayashi K, Weiland D, Vidali S, et al. Mitochondrial function in murine skin epithelium is crucial for hair follicle morphogenesis and epithelial-mesenchymal interactions. J Invest Dermatol 2015;135:679–89.

Knuever J, Poeggeler B, Gáspár E, Klinger M, Hellwig-Burgel T, Hardenbicker C, et al. Thyrotropin-releasing hormone controls mitochondrial biology in human epidermis. J Clin Endocrinol Metab 2012;97:978–86.

Kumar A, Vaish M, Karuppagounder SS, Gazaryan I, Cave JW, Starkov AA, et al. HIF1α stabilization in hypoxia is not oxidant-initiated. eLife 2021;10:e72873.

Lee P, Chandel NS, Simon MC. Cellular adaptation to hypoxia through hypoxia inducible factors and beyond. Nat Rev Mol Cell Biol 2020;21:268–83.

Mahfouf W, Hosseini M, Muzotte E, Serrano-Sanchez M, Dousset L, Moisan F, et al. Loss of epidermal HIF-1α blocks UVB-induced tumorigenesis by affecting DNA repair capacity and oxidative stress. J Invest Dermatol 2019;139:2016–28.e7.

Pappas A. Epidermal surface lipids. Dermatoendocrinol 2009;1:72–6.

Paus R, Bodó E, Kromminga A, Jelkmann W. Erythropoietin and the skin: a role for epidermal oxygen sensing? BioEssays 2009;31:344–8.

Rasmussen P, Nordsborg N, Taudorf S, Sørensen H, Berg RM, Jacobs RA, et al. Brain and skin do not contribute to the systemic rise in erythropoietin during acute hypoxia in humans. FASEB J 2012;26:1831–4.

Rezvani HR, Ali N, Nissen LJ, Harfouche G, De Verneuil H, Taïeb A, et al. HIF-1α in epidermis: oxygen sensing, cutaneous angiogenesis, cancer, and non-cancer disorders. J Invest Dermatol 2011a;131:1793–805.

Rezvani HR, Ali N, Serrano-Sanchez M, Dubus P, Varon C, Ged C, et al. Loss of epidermal hypoxia-inducible factor-1α accelerates epidermal aging and affects re-epithelialization in human and mouse. J Cell Sci 2011b;124:4172–83.

Ronquist G, Andersson A, Bendsoe N, Falck B. Human epidermal energy metabolism is functionally anaerobic. Exp Dermatol 2003;12:572–9.

Rosenberger C, Solovan C, Rosenberger AD, Jinping L, Treudler R, Frei U, et al. Upregulation of hypoxia-inducible factors in normal and psoriatic skin. J Invest Dermatol 2007;127:2445–52.

Ryan DG, Murphy MP, Frezza C, Prag HA, Chouchani ET, O'Neill LA, et al. Coupling Krebs cycle metabolites to signalling in immunity and cancer. Nat Metab 2019;1:16–33.

Schofield CJ, Ratcliffe PJ. Oxygen sensing by HIF hydroxylases. Nat Rev Mol Cell Biol 2004;5:343–54.

Segre JA. Epidermal barrier formation and recovery in skin disorders. J Clin Invest 2006;116:1150–8.

Semenza GL. Regulation of oxygen homeostasis by hypoxia-inducible factor 1. Physiology (Bethesda) 2009;24:97–106.

Semenza GL. Hypoxia-inducible factors in physiology and medicine. Cell 2012;148:399–408.

Stücker M, Struk A, Altmeyer P, Herde M, Baumgärtl H, Lübbers DW. The cutaneous uptake of atmospheric oxygen contributes significantly to the oxygen supply of human dermis and epidermis. J Physiol 2002;538:985–94.

Stücker M, Struk PA, Hoffmann K, Schulze L, Röchling A, Lübbers DW. The transepidermal oxygen flux from the environment is in balance with the capillary oxygen supply. J Invest Dermatol 2000;114:533–40.

Takagi S, Tojo H, Tomita S, Sano S, Itami S, Hara M, et al. Alteration of the 4-sphingenine scaffolds of ceramides in keratinocyte-specific Arnt-deficient mice affects skin barrier function. J Clin Invest 2003;112:1372–82.

van Smeden J, Bouwstra JA. Stratum corneum lipids: their role for the skin barrier function in healthy subjects and atopic dermatitis patients. Curr Probl Dermatol 2016;49:8–26.

Velarde MC. Epidermal barrier protects against age-associated systemic inflammation. J Invest Dermatol 2017;137:1206–8.

Wallace DC. Mitochondria and cancer. Nat Rev Cancer 2012;12:685–98.

Wang G, Sweren E, Andrews W, Li Y, Chen J, Xue Y, et al. Commensal microbiome promotes hair follicle regeneration by inducing keratinocyte HIF-1α signaling and glutamine metabolism. Sci Adv 2023;9:eabo7555.

Weiland D, Brachvogel B, Hornig-Do HT, Neuhaus JFG, Holzer T, Tobin DJ, et al. Imbalance of mitochondrial respiratory chain complexes in the epidermis induces severe skin inflammation. J Invest Dermatol 2018;138:132–40.

Wenger RH, Kurtcuoglu V, Scholz CC, Marti HH, Hoogewijs D. Frequently asked questions in hypoxia research. Hypoxia (Auckl) 2015;3:35–43.

Williams NC, Ryan DG, Costa ASH, Mills EL, Jedrychowski MP, Cloonan SM, et al. Signaling metabolite L-2-hydroxyglutarate activates the transcription factor HIF-1α in lipopolysaccharide-activated macrophages. J Biol Chem 2022;298:101501.

Yogev O, Yogev O, Singer E, Shaulian E, Goldberg M, Fox TD, et al. Fumarase: a mitochondrial metabolic enzyme and a cytosolic/nuclear component of the DNA damage response. PLoS Biol 2010;8:e1000328.

SUPPLEMENTARY RESULTS

The aerobic–glycolytic phenotype of wild-type keratinocytes was confirmed by measuring extracellular acidification rate (analogous to lactate production) (Supplementary Figure S3a), where keratinocytes produced 3 times more lactate than dermal fibroblasts. However, keratinocytes also consumed 75% more oxygen (Supplementary Figure S3b), consequently showing a 75% higher rate of adenosine triphosphate production by oxidative phosphorylation (Supplementary Figure S2c–f) to support their higher proliferation rate.

Our measurements show that both the basal and the maximally possible respiration rates were higher in keratinocytes (Supplementary Figure S3e and f), indicating that proliferating keratinocytes have a high energy demand, which they cover in large part by oxidative phosphorylation. Interestingly, nonmitochondrial oxygen consumption is also increased in keratinocytes compared with that in fibroblasts (Supplementary Figure S3c).

SUPPLEMENTARY MATERIALS AND METHODS

Animal generation and experiments

Keratin 14-Cre (Hafner et al, 2004), R26-K320E-Twinkle$^{loxP/loxP}$ (Baris et al, 2015), and Hif1a$^{loxP/loxP}$ (Boutin et al, 2008) mice were previously described. K320E-Twinkle^{epi} mice, called Twinkle^{epi} mice in this study (K14-Cre$^{+/-}$; K320E-Twinkle$^{loxP/wt}$), were generated as previously described (Weiland et al, 2018). K320E-Twinkle-Hif1a^{epi} mice (K14-Cre$^{+/-}$; K320E-Twinkle$^{loxP/wt}$; Hif1a$^{loxP/loxP}$) and Hif1a^{epi} mice (K14-Cre$^{+/-}$; Hif1a$^{loxP/loxP}$) were generated by crossing these mouse lines. Littermates with the same genotype but lacking Cre recombinase were used as controls. Genotyping was performed on tail or ear biopsies using primers available upon request. Where indicated, embryos were obtained by cesarean section.

Measurements of blood glucose and lactate levels

Blood glucose and lactate levels were measured in serum, freshly prepared from blood of newborn mice using the Cobas C 702 system (Roche Diagnostics, Indianapolis, IN) and the Radiometer ABL 800 Flex blood gas analyzer (Radiometer America, Brea, CA).

Tissue collection and histological and immunohistochemical analyses

Back and ventral skin samples from mice were embedded at the indicated time points in optimal cutting temperature compound (Tissue-Tek; Sakura, Alpen aan den Rijn, The Netherlands) or fixed in 4% paraformaldehyde and embedded in paraffin. H&E staining was performed on 5-μm slides to assess skin morphology. Epidermal and dermal thickness was measured using ImageJ software (ImageJ software, version 1.52, National Institutes of Health, Bethesda, MD). At least 5 randomized areas of each section were chosen (Leica SCN400 Slidescanner and Leica SlidePath Gateway Client LAN 2b4 Software, Leica Microsystems, Wetzlar, Germany), and 5–10 measurements were performed in each area. Giemsa staining and quantification (ImageJ software, version 1.52) were used for mast cell numbers. For immunostaining, endogenous peroxidase activity was blocked in paraffin sections with methanol:hydrogen peroxide (29:1), followed by overnight incubation at 4 °C in 5% fetal bovine serum and primary antibodies against keratin 14 (1:2000, 905301, BioLegend, Waltham, CA), keratin 10 (1:2000, 905401, BioLegend), loricrin (1:2000, 905101, BioLegend), FLG (1:1000, B257576, BioLegend), and Ki-67 (1:100, M7249, Dako, Vector Laboratories, Burlingame, CA). Slides were washed with PBS and then incubated with biotin-conjugated secondary antibodies for 1 hour. The reaction was visualized with the avidin-biotin complex kit (Dako, Vectastain Elite; Vector Laboratories) using diaminobenzidine for peroxidase reaction. Slides were counterstained with hematoxylin and mounted. Positive Ki-67 nucleus quantification was performed counting the positive nuclei per visual field in the basal epidermal layer in 5–8 random areas per section. For quantification of keratin 14, keratin 10, loricrin, and FLG expression in the epidermis, the corresponding layers were manually marked, respectively. After inverting to gray–white scales, the mean staining intensity was measured by ImageJ. Epidermal sheets were prepared by incubating skin in 1 mg/ml Dispase II (Roche, Basel, Switzerland) for 1 hour at room temperature, separating them from the dermis and then snap freezing for follow-up analyses.

Immunofluorescence

Immunofluorescence experiments were performed as previously described (Boix et al, 2016) using F4/80 (1:100, MCA497, Bio-Rad Laboratories, Hercules, CA) as primary antibody for the detection of macrophages and caspase-3 (1:200, 9664S, Cell Signaling Technology, Danvers, MA) for detection of apoptotic cells. Nile-red staining (0.1%, Sigma-Aldrich, St. Louis, MO) was performed for 5 minutes together with DAPI at room temperature. Pictures were taken at ×40 magnification with the Leica TCS SP8 microscope (Leica Microsystems). For the polar lipids, mean fluorescence intensity was measured from the preselected stratum corneum area (ImageJ software, version 1.52).

Quantification of mtDNA copy number

Total DNA was extracted with the DNeasy Blood & Tissue Kit (Qiagen, Hilden, Germany). The mtDNA copy number was measured by qPCR as previously described (Neuhaus et al, 2017).

Isolation and culture of primary keratinocytes and fibroblasts

Keratinocytes and fibroblasts were isolated from newborn mouse skin after epidermal–dermal separation by overnight incubation in 5 mg/ml Dispase II (Roche) at 4 °C as previously described (Rübsam et al, 2017) and dermal digestion by collagenase at 37 °C. Standard conditions for primary cells were set at 32 °C (keratinocytes) and 37 °C (fibroblasts) and 5% carbon dioxide in DMEM/HAM's F12 (FAD) medium with low calcium ion (50 μM) (Merck Millipore, Burlington, MA) supplemented with 10% fetal calf serum (chelated), penicillin (100 U ml^{-1}), streptomycin (100 μg ml^{-1}, Biochrom A2212, Merck Millipore), adenine (1.8 × 10^{-4} M, A3159, Sigma-Aldrich), L-glutamine (2 mM, Biochrom K0282, Merck Millipore), hydrocortisone (0.5 μg ml^{-1}, Sigma-Aldrich, H4001), epidermal GF (10 ng ml^{-1}, Sigma-Aldrich, E9644), cholera enterotoxin (10^{-10} M, Sigma-Aldrich, C-8052), insulin

(5 μg ml^{-1}, Sigma-Aldrich, I1882), and ascorbic acid (0.05 mg ml^{-1}, Sigma-Aldrich, A4034). For normoxic and hypoxic (1% oxygen partial pressure) conditions, keratinocytes were incubated for 6 hours at 37 °C. Wild-type keratinocytes were plated onto normal and gas-permeable Petriperm cell culture dishes, both in increasing density of 1, 2, and 4 million cells per well. ROS scavenger treatment was performed on cultured wild-type keratinocytes for 1, 4, and 24 hours with 2.5 mM each N-acetyl cysteine and 200 μM trolox.

RNA isolation and qRT-PCR

Epidermal and dermal sheets from newborn mice were homogenized using a mixer mill (Retsch, 5 minutes, 30 Hz). Total RNA was then isolated using Trizol (Thermo Fisher Scientific, Waltham, MA). cDNA was synthesized using the RevertAid First Strand cDNA Synthesis Kit (Thermo Fisher Scientific). qRT-PCR was performed using specific oligonucleotides (available upon request) and Power SYBR Green PCR Master Mix (Applied Biosystem, Waltham, MA) in an Applied Biosystems StepOnePlus Real Time PCR system. At least 3 biological replicates were used for each experimental group, and technical triplicates were assessed to calculate the mean value ± SD.

Immunoblotting

Whole-protein lysates from epidermal and dermal sheets were prepared and separated by SDS-PAGE as described (Baris et al, 2011). Whole-cell extracts of keratinocytes and fibroblasts were prepared as described (Fuhrmann et al, 2015; Müller-Edenborn et al, 2015). Primary antibodies were derived against HIF-1a (1:500, GTX127309, GeneTex or 1:500, 36169, Cell Signaling Technology), PHD2 (1:1000, 19886-1-AP, ProteinTech), PHD3 (1:1000, NB-100-139, Novus Biological), total protein kinase B (1:1000, 9272, Cell Signaling Technology), phosphorylated protein kinase B (1:500, 9271, Cell Signaling Technology), total oxidative phosphorylation Rodent WB Antibody Cocktail (1:4000, ab110413, Abcam, Cambridge, England), p70 (1:2000, 459200, Invitrogen), mtCO3 (1:2000, ab110259), tubulin (1:2000, T4026, Sigma-Aldrich), β-actin (1:5000, A1978, Sigma-Aldrich), vinculin (1:5000, 66305-1-Ig, ProteinTech), and GAPDH (1:5000, AB2302, Merk Millipore). Signals were detected using the Western Lightning Plus-ECL, Enhanced Chemiluminescence Substrate (PerkinElmer, Waltham, MA), and ImageQant LAS500 chemiluminescence CCD Camera (GE Healthcare Bio-Sciences, Pittsburgh, PA).

Cytokine profiling

Blood samples were centrifuged at 1500*g* and 4 °C for 10 minutes; the plasma was collected and stored at −20 °C until usage. Cytometric Bead Array Detection System using Mouse/Rat Soluble Protein Master Buffer Kit (catalog number 558266) was applied to measure IL-6 (Mouse Flex Set, catalog number 558301) levels in serum samples, according to the manufacturer's instructions. Measurements were performed using the FACSCanto II flow cytometer, and data were analyzed using the FCAP Array v3 software (BD) (Probst et al, 2018).

Epidermal barrier function assays

Epidermal dye permeability assays were performed with 1% toluidine blue dye (Sigma-Aldrich) at the indicated ages as described (Byrne et al, 2010). Transepidermal water loss was measured in newborn ventral skin using a Tewameter (Courage) and performed according to the manufacturer's instructions.

Energy metabolism

To characterize their energy metabolism, oxygen consumption rate and extracellular acidification rate were measured in keratinocytes and fibroblasts (so-called mito stress test; Seahorse XF96 Bioanalyzer). Cells were seeded at a density of 15,000 cells per well (n = 8). Prior to the assay, the cells were washed carefully with Seahorse assay media supplemented with glucose, sodium pyruvate, and L-glutamine. The cells were then allowed to adapt to the assay medium (XF Base Media Minimal DMEM, pH 7.4, supplemented with 10 mM glucose, 1 mM pyruvate, and 2 mM glutamine) for 1 hour. To characterize respiratory chain function, oligomycin was injected (1 μM), followed by FCCP (carbonyl cyanide p-trifluoromethoxyphenylhydrazone) (2 μM FCCP) and rotenone/antimycin A (0.5μM each). Then, Hoechst dye was added, and cells were counted 25 minutes later using an automated cell imaging software (Agilent). Oxygen consumption rate and extracellular acidification rate data were normalized to the number of living cells per well; 8 technical replicates were averaged to get the final graphs.

Anion-exchange chromatography mass spectrometry

Freshly isolated keratinocytes were seeded in collagen-coated plates 1 day before metabolite isolation. Cells were washed twice with PBS and incubated with precooled extraction buffer (methanol:acetonitrile:water, 40:40:20) at −20 °C for 10 minutes. Samples were collected using a cell scraper, and the extraction was repeated using the same extraction buffer. Fresh frozen epidermal tissue was homogenized using a ball mill (Retsch MM400) after precooling the samples in the holder with liquid nitrogen. Extraction buffer was the same as described earlier. Proteins were spun down by centrifugating samples at 21,000*g* for 10 minutes, and the supernatant was used as follows. Extracted metabolites were resuspended in 150 μl of ultra-performance liquid chromatography mass spectrometry grade water (Biosolve), of which 100 μl were transferred to polypropylene autosampler vials (Chromatography Accessories Trott, Kriftel, Germany) before anion-exchange chromatography mass spectrometry analysis. The samples were analyzed using a Dionex ion chromatography system (Integrion, Thermo Fisher Scientific) as described previously (Schwaiger et al, 2017). In brief, 5 μl of polar metabolite extract were injected in push partial mode, using an overfill factor of 1, onto a Dionex IonPac AS11- HC column (2 mm × 250 mm, 4 μm particle size, Thermo Fisher Scientific) equipped with a Dionex IonPac AG11-HC guard column (2 mm × 50 mm, 4 μm, Thermo Fisher Scientific). The column temperature was held at 30 °C, whereas the auto sampler was set to 6 °C. A potassium hydroxide gradient was generated using a potassium hydroxide cartridge (Eluent Generator, Thermo Scientific Scientific), which was supplied with deionized water (Merck Millipore). The metabolite separation was carried at a flow rate of 380 μl/min, applying the following gradient conditions: 0−3 minutes, 10 mM potassium hydroxide; 3−12 minutes, 10−50 mM potassium hydroxide; 12−19 minutes, 50−100 mM potassium

hydroxide; 19−22 minutes, 100 mM potassium hydroxide, and 22−23 minutes, 100−10 mM potassium hydroxide. The column was re-equilibrated at 10 mM for 3 minutes. For the analysis of metabolic pool sizes, the eluting compounds were detected in negative ion mode using full scan measurements in the mass range of m/z 77−770 on a Q-Exactive HF high resolution mass spectrometer (Thermo Fisher Scientific). The heated electrospray ionization source settings of the mass spectrometer were Spray voltage 3.2 kV, capillary temperature set to 300 °C, sheath gas flow of 50 AU, aux gas flow of 20 AU at a temperature of 330 °C, and a sweep gas glow of 2 AU. The S-lens was set to a value of 60. The semitargeted liquid chromatography mass spectrometry data analysis was performed using the TraceFinder software (version 4.1, Thermo Fisher Scientific). The identity of each compound was validated by authentic reference compounds, which were measured at the beginning and the end of the sequence. For data analysis, the area of the deprotonated [M-H+]-1 or doubly deprotonated [M-2H]-2 monoisotopologue mass peaks of every required compound were extracted and integrated using a mass accuracy <5 ppm and a retention time tolerance of <0.05 minutes compared with the independently measured reference compounds. These areas were then normalized to the internal standards, which were added to the extraction buffer, followed by a normalization to the fresh weight of the analyzed sample. Five replicates were used. The ratios between a-ketoglutarate and succinate, fumarate, 2-OH-glutarate, or lactate were calculated with the mean of all replicates.

Statistics

Experimental data were analyzed using GraphPad Prism 8.0 (GraphPad Software Ink). Unless otherwise mentioned, mean values ± SD are shown. For comparisons between 2 experimental groups, we used Student's unpaired 2-tailed *t*-test. For comparisons among >2 experimental groups, 1-way ANOVA was used, which if statistically significant was followed by a posthoc Tukey's multiple comparison test. $P < .05$ was considered statistically significant. $^{*}P < .05$, $^{**}P < .01$, and $^{***}P < .001$. When normality of distribution could not be assessed because of limited size of some sample groups (n = 3−8), statistical analysis was performed with the assumption of normally distributed data.

SUPPLEMENTARY REFERENCES

Baris OR, Ederer S, Neuhaus JF, von Kleist-Retzow JC, Wunderlich CM, Pal M, et al. Mosaic deficiency in mitochondrial oxidative metabolism promotes cardiac arrhythmia during aging. Cell Metab 2015;21:667−77.

Baris OR, Klose A, Kloepper JE, Weiland D, Neuhaus JF, Schauen M, et al. The mitochondrial electron transport chain is dispensable for proliferation and differentiation of epidermal progenitor cells. Stem Cells 2011;29:1459−68.

Boix J, Sevilla LM, Sáez Z, Carceller E, Pérez P. Epidermal mineralocorticoid receptor plays beneficial and adverse effects in skin and mediates glucocorticoid responses. J Invest Dermatol 2016;136:2417−26.

Boutin AT, Weidemann A, Fu Z, Mesropian L, Gradin K, Jamora C, et al. Epidermal sensing of oxygen is essential for systemic hypoxic response. Cell 2008;133:223−34.

Byrne C, Avilion AA, O'Shaughnessy RF, Welti JC, Hardman MJ. Whole-mount assays for gene induction and barrier formation in the developing epidermis. Methods Mol Biol 2010;585:271−86.

Fuhrmann DC, Tausendschön M, Wittig I, Steger M, Ding MG, Schmid T, et al. Inactivation of tristetraprolin in chronic hypoxia provokes the expression of cathepsin B. Mol Cell Biol 2015;35:619−30.

Hafner M, Wenk J, Nenci A, Pasparakis M, Scharffetter-Kochanek K, Smyth N, et al. Keratin 14 Cre transgenic mice authenticate keratin 14 as an oocyte-expressed protein. Genesis 2004;38:176−81.

Müller-Edenborn K, Léger K, Glaus Garzon JF, Oertli C, Mirsaidi A, Richards PJ, et al. Hypoxia attenuates the proinflammatory response in colon cancer cells by regulating IκB. Oncotarget 2015;6:20288−301.

Neuhaus JF, Baris OR, Kittelmann A, Becker K, Rothschild MA, Wiesner RJ. Catecholamine metabolism induces mitochondrial DNA deletions and leads to severe adrenal degeneration during aging. Neuroendocrinology 2017;104:72−84.

Probst K, Stermann J, von Bomhard I, Etich J, Pitzler L, Niehoff A, et al. Depletion of collagen IX Alpha1 impairs myeloid cell function. Stem Cells 2018;36:1752−63.

Rübsam M, Mertz AF, Kubo A, Marg S, Jüngst C, Goranci-Buzhala G, et al. E-cadherin integrates mechanotransduction and EGFR signaling to control junctional tissue polarization and tight junction positioning. Nat Commun 2017;8:1250.

Schwaiger M, Rampler E, Hermann G, Miklos W, Berger W, Koellensperger G. Anion-exchange chromatography coupled to high-resolution mass spectrometry: a powerful tool for merging targeted and non-targeted metabolomics. Anal Chem 2017;89:7667−74.

Weiland D, Brachvogel B, Hornig-Do HT, Neuhaus JFG, Holzer T, Tobin DJ, et al. Imbalance of mitochondrial respiratory chain complexes in the epidermis induces severe skin inflammation. J Invest Dermatol 2018;138:132−40.

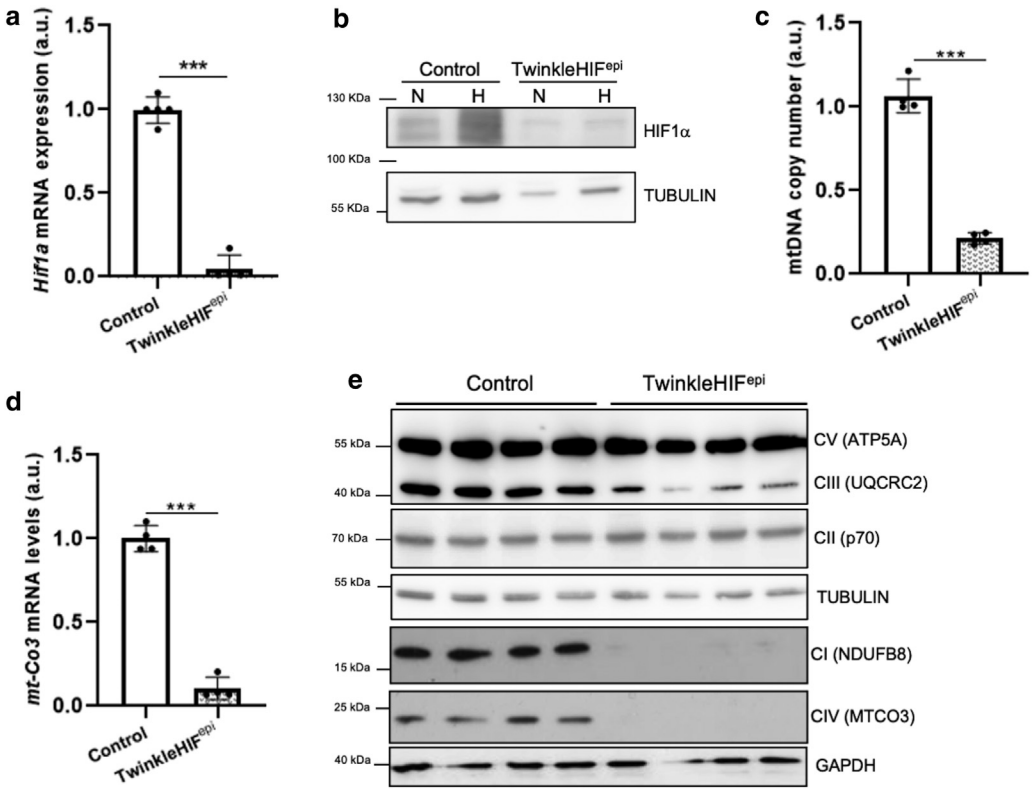

Supplementary Figure S1. Successful *knock-out* of HIF-1α, mtDNA depeletion and decreased expression of respiratory chain complexes in TwinkleHIF^{epi} mice. (**a**) RT-qPCR showing *Hif1a* mRNA levels in control and TwinkleHIF^{epi} newborn epidermis at birth (n = 4–5 mice per genotype). (**b**) Representative immunoblot of HIF-1a protein in control and TwinkleHIF^{epi} epidermal keratinocytes isolated and cultured in normoxic (denoted as N, 21% O_2, 6 h) or hypoxic (denoted as H, 1% O_2, 6 h) conditions. Tubulin was used as loading control. (**c**) qPCR for mtDNA copy number quantification in control and TwinkleHIF^{epi} epidermis at birth (n = 3–4 mice per genotype). (**d**) RT-qPCR showing *mt-Co3* mRNA levels in control and TwinkleHIF^{epi} newborn epidermis at birth (n = 4 mice per genotype). (**e**) Immunoblot of representative subunits (in brackets) of the 5 OXPHOS complexes (denoted as C) in control and TwinkleHIF^{epi} epidermis of newborn mice. Tubulin or GAPDH were used as loading controls according to molecular weight. Data are presented as mean ± SD (for **a, c,** and **d**) and analyzed with Student's *t*-test. $^{**}P < .01$ and $^{***}P < .001$. a.u., arbitrary unit; h, hour; O_2, oxygen; OXPHOS, oxidative phosphorylation.

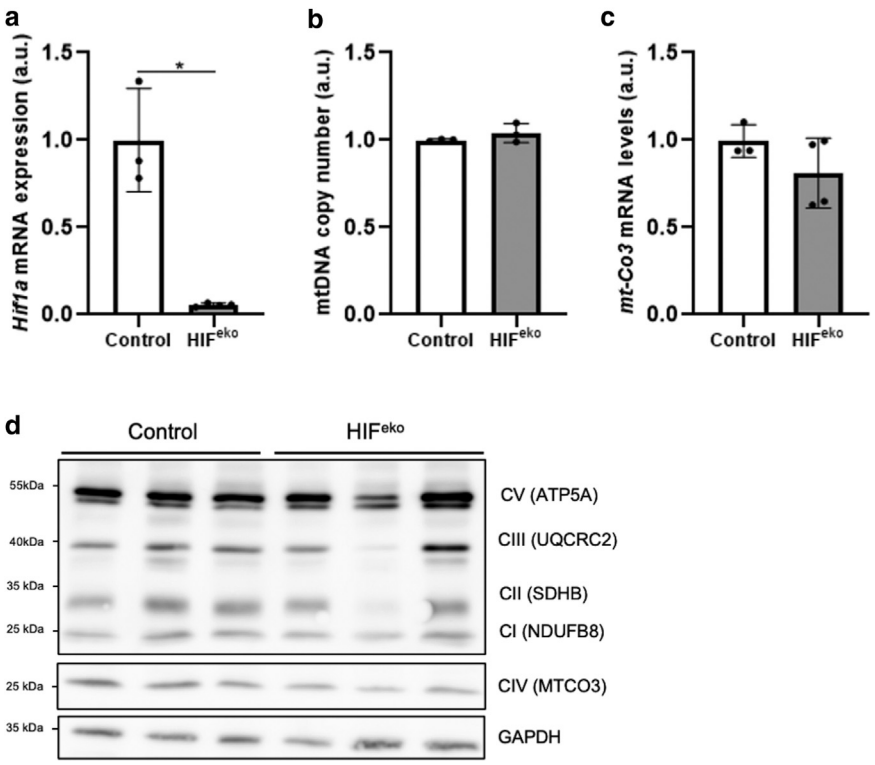

Supplementary Figure S2. Successful *knock-out* of HIF-1α, unaltered mtDNA levels and normal stoichiometry of respiratory chain complexes in HIF^{eko} mice. (**a**) RT-qPCR showing *Hif1a* mRNA levels in control and HIF^{eko} newborn epidermis at birth (n = 3−4 mice per genotype). (**b**) qPCR for mtDNA copy number quantification in control and HIF^{eko} epidermis at birth (n = 3 mice per genotype). (**c**) RT-qPCR showing *mt-Co3* mRNA levels in control and HIF^{eko} newborn epidermis at birth (n = 3−4 mice per genotype). (**d**) Immunoblot of representative subunits (in brackets) of the 5 OXPHOS complexes (denoted as C) in control and HIF^{eko} epidermis of newborn mice. GAPDH was used as loading control. Data are presented as mean ± SD (for **a**−**c**) and analyzed with Student's *t*-test. *$P < .05$. a.u., arbitrary unit; OXPHOS, oxidative phosphorylation.

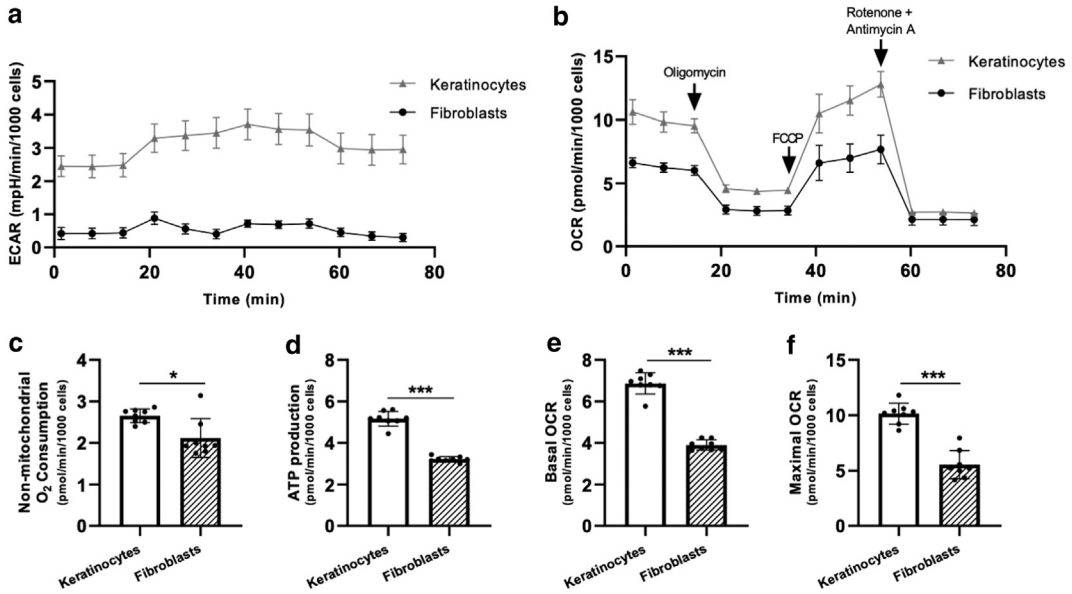

Supplementary Figure S3. Wild-type keratinocytes cultured *in vitro* are energetically more active than fibroblast. Graphs displaying (**a**) ECAR, (**b**) OCR, and (**c**–**f**) derived bioenergetic parameters of primary keratinocytes and fibroblasts in culture (n = 8 biological replicates per cell type). For interpretation, see Supplementary Results section. Data are presented as mean ± SD (for **c**–**f**) and analyzed with Student's *t*-test. *$P < .05$ and ***$P < .001$. ECAR, extracellular acidification rate; OCR, oxygen consumption rate.

Supplementary Figure S4. Dermal thickness and filaggrin expression are not affected by the absence of HIF-1α or functional mitochondria. (**a**) Dermal thickness of control, HIF^{eko}, Twinkle^{epi}, and TwinkleHIF^{epi} newborn skin at birth (n = 3–4 mice per genotype). (**b**) Epidermal thickness of control and HIF^{eko} adult mice (n = 3 mice per genotype). (**c**) Immunostaining and quantification of FLG of control (n = 5), HIF^{eko} (n = 4), Twinkle^{epi} (n = 3), and TwinkleHIF^{epi} (n = 4) newborn skin at birth. Bar = 100 μm. Data are presented as mean ± SD (for **a**–**c**). DAB, 3,3′-diaminobenzidine.

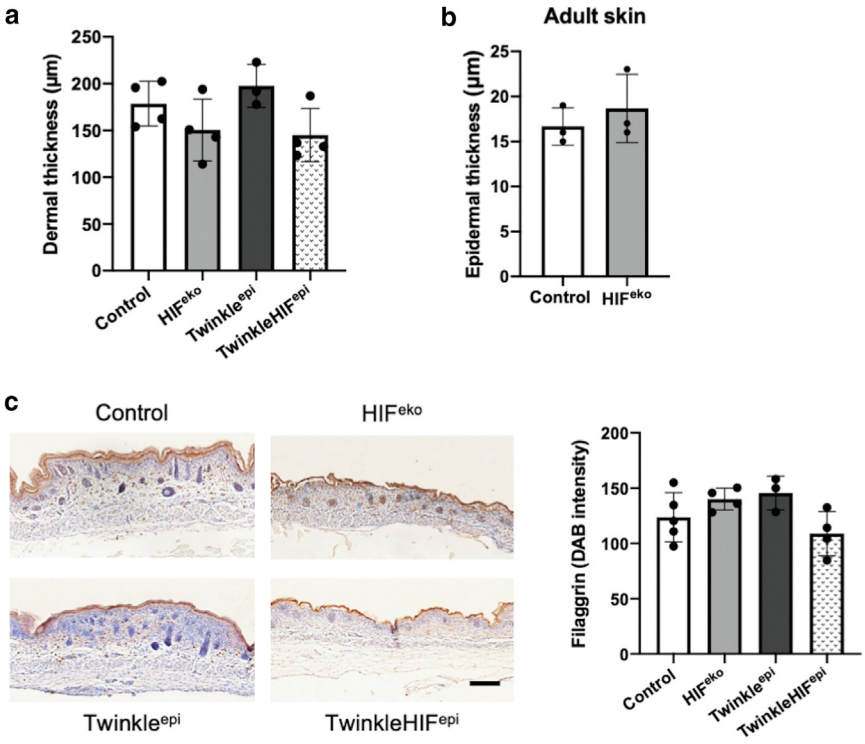

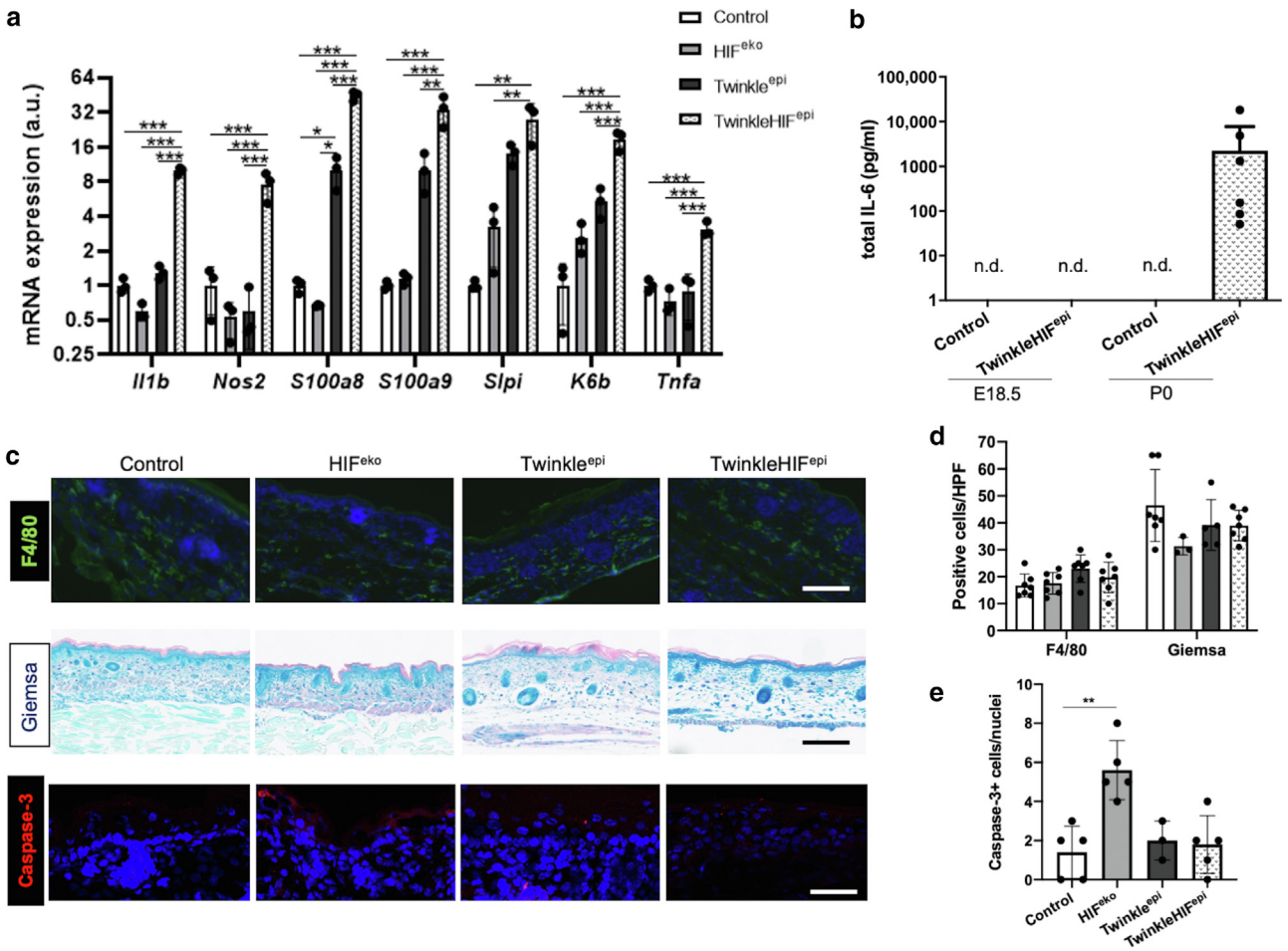

Supplementary Figure S5. The inflammatory response induced by mitochondrial dysfunction is exaggerated in the absence of HIF-1α. (**a**) RT-qPCR showing mRNA levels for *Il1b, Nos2, S100a8, S100a9, Slpi, K6b,* and *Tnfa* in control; HIF^{eko}; Twinkle^{epi}; and TwinkleHIF^{epi} newborn epidermis (n = 3 mice per genotype). (**b**) Total IL-6 levels measured in control (n = 3) and TwinkleHIF^{epi} (n = 12) serum at E18.5 and birth. Nondetectable levels were indicated as n.d. (**c**) Immunofluorescence for F4/80 (macrophages) (bar = 50 μm), Giemsa staining (mast cells) (bar = 100 μm), and immunofluorescence of caspase-3–positive cells in control; HIF^{eko}; Twinkle^{epi}; and TwinkleHIF^{epi} newborn skin. Bar = 100 μm. (**d**) Quantification of macrophages and mast cells (n = 3–7 mice per genotype). (**e**) Quantification of caspase-3–positive cells (n = 3–5 mice per genotype). Data are presented as mean ± SD (for **a**–**e**) and analyzed with 1-way ANOVA, Tukey's posthoc test. *$P < .05$, **$P < .01$, and ***$P < 0.001$. a.u., arbitrary unit; E18.5, embryonic day 18.5; HPF, high-power field; Nos2, nitric oxide synthase 2.

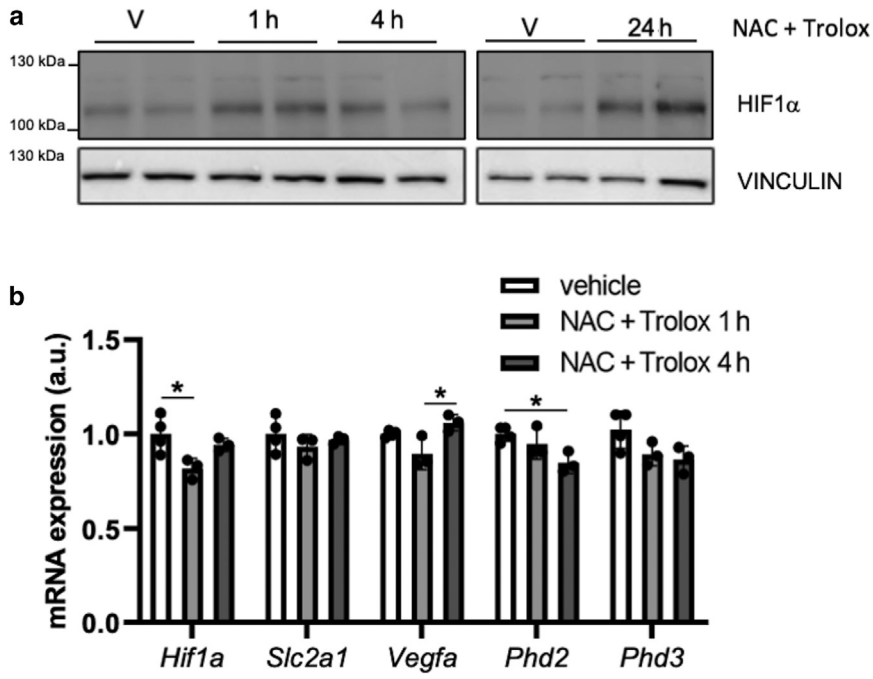

Supplementary Figure S6. HIF-1α stabilization is not mediated via ROS in wild-type keratinocytes. (**a**) Representative immunoblot of HIF-1a in keratinocytes treated with vehicle (denoted as V) or ROS scavengers for the indicated time. Vinculin was used as high-molecular-weight loading control. (**b**) RT-qPCR showing *Hif1a*, *Slc2a1*, *Vegfa*, *Phd2*, and *Phd3* mRNA levels in wild-type keratinocytes treated with vehicle or ROS scavengers for the indicated time. Data are presented as mean ± SD and analyzed with 1-way ANOVA, Tukey's posthoc test. $*P < .05$. a.u., arbitrary unit; h, hour; NAC, N-acetylcystein.